Remote Sensing of Environment 256 (2021) 112275

Contents lists available at ScienceDirect

Remote Sensing of Environment

journal homepage: www.elsevier.com/locate/rse

Air pollution trends measured from Terra: CO and AOD over industrial, fire-prone, and background regions

Rebecca R. Buchholz [a,*], Helen M. Worden [a], Mijeong Park [a], Gene Francis [a], Merritt N. Deeter [a], David P. Edwards [a], Louisa K. Emmons [a], Benjamin Gaubert [a], John Gille [a], Sara Martínez-Alonso [a], Wenfu Tang [a,b], Rajesh Kumar [c], James R. Drummond [d,m], Cathy Clerbaux [e,f], Maya George [e], Pierre-François Coheur [f], Daniel Hurtmans [f], Kevin W. Bowman [g,h], Ming Luo [g], Vivienne H. Payne [g], John R. Worden [g], Mian Chin [i], Robert C. Levy [i], Juying Warner [j], Zigang Wei [k], Susan S. Kulawik [l]

[a] Atmospheric Chemistry Observations & Modeling Laboratory, National Center for Atmospheric Research, Boulder, CO, USA
[b] Advanced Study Program, National Center for Atmospheric Research, Boulder, CO, USA
[c] Research Applications Laboratory, National Center for Atmospheric Research, Boulder, CO, USA
[d] University of Toronto, Toronto, Ontario, Canada
[e] LATMOS/IPSL, Sorbonne Université, UVSQ, CNRS, Paris, France
[f] Université libre de Bruxelles (ULB), Service de Chimie Quantique et Photophysique, Atmospheric Spectroscopy, Brussels, Belgium
[g] NASA Jet Propulsion Laboratory (JPL), Pasadena, CA, USA
[h] Joint Institute for Regional Earth System Science and Engineering (JIFRESSE), University of California, Los Angeles, CA, USA
[i] NASA/Goddard Space Flight Center (GSFC), Greenbelt, MD, USA
[j] Dept. of Atmospheric & Oceanic Science, University of Maryland, College Park, MD, USA
[k] IMSG, Inc. at NOAA/NESDIS Center for Satellite Applications and Research (STAR), College Park, MD, USA
[l] NASA Ames Research Center, Moffett Field, CA, USA
[m] Dalhousie University, Halifax, Nova Scotia, Canada

ARTICLE INFO

Keywords:
Carbon monoxide
AOD
NASA/Terra satellite
Trend
Interannual variability

ABSTRACT

Following past studies to quantify decadal trends in global carbon monoxide (CO) using satellite observations, we update estimates and find a CO trend in column amounts of about −0.50 % per year between 2002 to 2018, which is a deceleration compared to analyses performed on shorter records that found −1 % per year. Aerosols are co-emitted with CO from both fires and anthropogenic sources but with a shorter lifetime than CO. A combined trend analysis of CO and aerosol optical depth (AOD) measurements from space helps to diagnose the drivers of regional differences in the CO trend. We use the long-term records of CO from the Measurements of Pollution in the Troposphere (MOPITT) and AOD from the Moderate Resolution Imaging Spectroradiometer (MODIS) instrument. Other satellite instruments measuring CO in the thermal infrared, AIRS, TES, IASI, and CrIS, show consistent hemispheric CO variability and corroborate results from the trend analysis performed with MOPITT CO. Trends are examined by hemisphere and in regions for 2002 to 2018, with uncertainties quantified. The CO and AOD records are split into two sub-periods (2002 to 2010 and 2010 to 2018) in order to assess trend changes over the 16 years. We focus on four major population centers: Northeast China, North India, Europe, and Eastern USA, as well as fire-prone regions in both hemispheres. In general, CO declines faster in the first half of the record compared to the second half, while AOD trends show more variability across regions. We find evidence of the atmospheric impact of air quality management policies. The large decline in CO found over Northeast China is initially associated with an improvement in combustion efficiency, with subsequent additional air quality improvements from 2010 onwards. Industrial regions with minimal emission control measures such as North India become more globally relevant as the global CO trend weakens. We also examine the CO trends in monthly percentile values to understand seasonal implications and find that local changes in biomass burning are sufficiently strong to counteract the global downward trend in atmospheric CO, particularly in late summer.

* Corresponding author.
E-mail address: buchholz@ucar.edu (R.R. Buchholz).

https://doi.org/10.1016/j.rse.2020.112275
Received 21 December 2019; Received in revised form 15 October 2020; Accepted 20 December 2020
Available online 26 January 2021

1. Introduction

Carbon monoxide (CO) is an atmospheric tracer for incomplete combustion, with major primary sources from fossil fuels and fires and secondary production from hydrocarbon oxidation. CO is destroyed through photochemical oxidation and is the dominant sink for the hydroxyl radical (OH), thus impacting the self-cleansing capacity of the atmosphere (e.g., Lelieveld et al., 2016) and methane (CH4) lifetime (Prather, 2007; Gaubert et al., 2017a). CO is a short-lived climate pollutant (SLCP) via its impact on carbon dioxide and ozone formation, and the methane budget, with a radiative forcing of 0.23 Wm^{-2} (Myhre et al., 2014) but whose impact is sensitive to emission location (Bowman and Henze, 2012). The moderate CO lifetime of weeks to months (e.g., Holloway et al., 2000) allows for observation of distinct pollution plumes that gradually succumb to atmospheric mixing, making it useful for studying both pollution sources and atmospheric background loadings.

Tropospheric CO is accessible to remote sensing through its absorption of infrared radiation and is observed by several satellite instruments. The longest running satellite instrument is the Measurements Of Pollution In The Troposphere (MOPITT), aboard the NASA Terra satellite, which has been observing CO since 2000 (Drummond et al., 2010). A consistent record combined with recent algorithm improvements that minimize bias drift (Deeter et al., 2019) ensure that MOPITT CO is suitable for atmospheric trend calculations.

Atmospheric CO has been decreasing globally for the last two decades, primarily due to improvements in the combustion efficiency of anthropogenic sources, in addition to a global decline in tropical fires (Novelli et al., 2003; Zeng et al., 2012; Worden et al., 2013; Schultz et al., 2015; Yin et al., 2015; Jiang et al., 2017; Gaubert et al., 2017; Andela et al., 2017; Tang et al., 2019; Zheng et al., 2019). Recently, positive fire trends in Northern Hemisphere boreal regions (e.g., for the USA, Dennison et al., 2014) may have counteracted the globally decreasing CO. While trends in CO over fire-prone regions such as the Amazon and Southern Africa are more difficult to determine due to the large source interannual variability (Strode and Pawson, 2013), the CO record from MOPITT is potentially long enough to determine trends within this variability. Inverse modeling studies to estimate CO emissions and trends using MOPITT observations confirm reductions from fossil fuel combustion and tropical biomass burning (Jiang et al., 2017; Zheng et al., 2018b, 2019). Strode et al. (2016) show that accurate emissions and ozone chemistry are critical for model simulations that agree with observations and to interpret trends in CO concentrations. Additionally, changing air quality policies, such as the 2010 China Clean Air Policy (Zheng et al., 2018a), can reduce or increase pollution emissions with impacts on trends in atmospheric composition.

Atmospheric aerosols are also a marker of pollution processes. Fine particulate matter (diameter < 2.5 μm; PM2.5) has a significant negative impact on human health (e.g., McClure and Jaffe, 2018). Depending on type, aerosols can have either cooling or warming radiative forcing on climate (e.g., Ramanathan and Carmichael, 2008). Through impacting photolysis rates, aerosols can impact other pollutants such as ozone (Li et al., 2019). Previous studies have demonstrated that satellite observations of atmospheric aerosol along with CO can provide additional information in determining CO sources and understanding CO spatial and temporal variability (e.g., Edwards et al., 2004). The most reliable satellite observations are of bulk aerosol total column optical depth (AOD), and these are also available on Terra from the Moderate Resolution Imaging Spectroradiometer (MODIS) instrument. Of particular interest here are the organic carbon and black carbon aerosols that are directly emitted along with CO during the incomplete combustion of fossil fuels and biomass (e.g., Edwards et al., 2004; Arellano et al., 2010). However, distinguishing carbonaceous aerosol from other different aerosol types that contribute to the AOD, and especially the component from fine mode aerosol, is challenging. Aerosols are also formed from secondary reactions of pollutant precursor gases, and these may or may not originate from the same combustion sources as CO. For example, sulfate aerosol results from the oxidation of sulfur dioxide (SO_2), although the SO_2 emissions are not necessarily associated with CO sources. (e.g., Unger, 2006). Spatial correlation of MODIS AOD with short-lived species SO_2, nitrogen dioxide (NO_2) and formaldehyde has been used to suggest dominant aerosol types for different global regions (Veefkind et al., 2011).

The shorter lifetime of aerosols, ~ 4 to 12 days (e.g., Kanakidou et al., 2005) means that they are not observed as far away from sources as CO, so AOD trends are more indicative of local and regional behavior in air pollution. The economically developing regions of the Asian landmass and surrounding oceanic regions are reported to show increasing AOD from satellite-based measurements using MODIS and Multi-angle Imaging SpectroRadiometer (MISR) AOD, whereas North America, South America, and Europe show decreasing AOD (Mehta et al., 2016). Ground-based analysis also shows increases over India, for example, at a rate of 2.3% per year between 1985 and 2012 and at 4% per year since 2000 (Krishna Moorthy et al., 2013). In the US, air quality related to surface-measured aerosols (PM2.5) has been improving, as shown by a decreasing trend, except where there are fires in the northwest (McClure and Jaffe, 2018).

This paper presents the trends in CO measured from space between 2002 and 2018 and uses satellite-measured AOD to help understand CO variability. We split the records into two time periods to measure the trend temporal stability, as well as examine trends over different source and outflow regions, and analyze monthly percentile values. In Section 2 we present the CO and AOD satellite-based measurements and describe the trend analysis methodology. Section 3 shows the CO and AOD records across different spatial and temporal scales, including regional trends (Section 3.4). Section 4 discusses potential impacts on atmospheric trends by investigating the co-variation of CO and AOD, as well as monthly CO percentile data. Conclusions are presented in Section 5.

2. Methods

2.1. Long-term CO and AOD measured from space

The NASA/Terra satellite, launched in December 1999, carries two key instruments for the work of this paper, MOPITT and MODIS. Terra follows a sun-synchronous orbit with equator crossing times of ~10:30 local solar time (LST).

2.1.1. MOPITT CO

MOPITT is a nadir-viewing instrument that began measuring CO in 2000 and provides global coverage about every three days. The cross-track scanning angle is ±26 degrees to yield a swath width of ~640 km. Pixel resolution is ~22 km × 22 km at nadir. MOPITT uses gas correlation spectrometry to complete broadband measurements in the thermal infrared (TIR) near 2140 cm^{-1} and the near infrared (NIR) near 4275 cm^{-1} (Drummond et al., 2010). The MOPITT retrieval algorithm is described in detail elsewhere (Deeter et al., 2019; Worden et al., 2013). Briefly, an optimal estimation algorithm is applied to upwelling radiances, that have traveled through CO filled gas cells of varying lengths, to retrieve CO profiles of volume mixing ratio (VMR) on 10 vertical layers, which are integrated to provide reported column amounts. The recent version 8 (V8) algorithm includes: updates to the N_2 and H_2O spectroscopic data; accounting for temporal bias drift and water vapor in the radiance bias correction; and updating to MODIS cloud Collection version 6.1 to determine clear conditions. Validation covers a range of locations and shows minimal bias drift for column amounts (Buchholz et al., 2017; Deeter et al., 2019). Improvements in retrieval stability for the V8 daytime retrievals result in a negligible drift of -0.015 ± 0.061% per year relative to NOAA airborne flask-sampling for CO total column over the MOPITT mission (Deeter et al., 2019).

While including NIR channel information in the retrievals enhances MOPITT sensitivity to CO in the lower troposphere, we use the TIR-only

product in order to compare with other TIR instruments (AIRS, TES, IASI, CrIS, introduced below). We use V8, TIR, daytime retrievals over land and/or ocean scenes, depending on the region of interest. Level-2 total column CO retrievals are used for regional trend analysis and monthly statistics (doi: 10.5067/TERRA/MOPITT/MOP02T_L2.008), while Level-3 monthly averaged total column CO is used for the global gridded trend and zonal average analyses (doi: 10.5067/TERRA/MOPITT/MOP03TM_L3.008). We filter Level-2 retrievals in the same way as Level-3, that is: anomaly diagnostics all must be false to remove negative Averaging Kernel elements and thermal anomalies; signal-to-noise in the 5A channel must be greater than 1000; and pixel 3 is removed because of the large noise variability (Deeter et al., 2015). Filtering in this way reduces inter-pixel differences (Hedelius et al., 2019). Data from 2002 onwards are used for trend analysis to avoid discontinuities with the early 2000–2001 data taken before the MOPITT cooler failure and instrumental reconfiguration that occurred in 2001 (Deeter et al., 2004).

2.1.2. MODIS AOD

As a passive imaging radiometer, MODIS measures reflected solar and thermal radiation in 36 bands with a 2330 km wide viewing swath, achieving near global coverage each day. At nadir view, spatial resolution is 1 km or finer, depending on the band. The calibration has been updated over time, mitigating an observed drift in radiance and reflectance due to sensor degradation.

The observed spectral reflectances are inverted to AOD values from look-up-tables that have been created with radiative transfer code that include different assumptions about surface properties and aerosol types. The DT algorithm (Levy et al., 2013) retrieves aerosol over open ocean and dark vegetated land surfaces while the DB retrieval algorithm adds retrievals over bright surfaces (Hsu et al., 2013). Both sets of algorithms report AOD at 0.55 μm along with quality assurance. Based upon selection of retrievals that pass recommended quality assurance (QA = 3, see Sayer et al., 2014), the merged Dark Target/Deep Blue (DTDB) product (Levy et al., 2013; Gupta et al., 2020), yields a single AOD value (at 10 km spatial resolution) in non-cloudy, non-ice/snow scenes. Aggregations of such 'Level 2' products onto daily and monthly 1°x1° grids lead to 'Level 3' products. MODIS Collection 6.1 (C6.1) represents a consistent reprocessing of all MODIS products, including original geolocation, calibration, aerosol retrieval, and Level 3 aggregation.

In this work, we have used the C6.1 monthly aggregations from MODIS-Terra known as MOD08_M3 (https://doi.org/10.5067/MODIS/MOD08_M3.061, Platnick et al., 2017). We use C6.1 because the previous Collection 6 (C6) showed some artifact trends (Levy et al., 2018) when compared to MODIS on Aqua (King et al., 2013). Since the calibration has been made consistent, C6.1 appears to be largely free of artificial drifts, which we have confirmed via comparisons with MODIS trends on Aqua (Supplementary Fig. C2). Wei et al. (2019a) also found C6.1 products were improved relative to C6. Wei et al. (2019b) found MODIS C6.1 performed best at capturing temporal variations and was closest to ground-based observations.

2.2. Other nadir-viewing, TIR satellite CO measurements

To assess the consistency of the hemispheric temporal variability of CO in Section 3.3, we compare data from a number of different nadir-viewing satellite instruments that make measurements in the TIR band of CO. All these instruments are onboard satellites with sun-synchronous orbits and, besides AIRS, use optimal estimation approaches to retrieve CO columns from measured radiances. Northern Hemisphere (NH) and Southern Hemisphere (SH) monthly averages are collated from each instrument. A summary of instrument specific details are given in Table 1.

2.2.1. AIRS

The Atmospheric Infrared Sounder (AIRS), on board NASA/Aqua was launched in 2002 and crosses the equator at ~13:15 LST (Aumann et al., 2003). Ground-pixel size is nominally 13.5 km × 13.5 km, but is degraded to 45 km × 45 km as a trade-off to increase global coverage using a cloud-clearing algorithm (Susskind et al., 2003). The 1650 km AIRS swath provides near global coverage twice daily. Radiance spectra from the AIRS grating spectrometer are used to determine cloud and surface properties along with vertical profiles of atmospheric trace gases (including CO at 4.6 μm) and temperature. Previous comparisons of AIRS and MOPITT CO showed good agreement in horizontal spatial variability, but found AIRS CO to be higher than MOPITT (V3) (Warner et al., 2007). However, the comparison in Worden et al. (2013), found better agreement using more recent versions of the retrieval algorithms for both instruments. We use the Level 2 V006 AIRS retrievals here, (AIRS2RET, AIRS Science Team/Joao Teixeira, 2013), which has 50 km x 50 km spatial resolution. The AIRS2RET Level 2 product was created Level-2 using AIRS IR-Only retrievals. NH and SH monthly average values were computed for daytime retrievals (SZA < 90).

2.2.2. IASI

There are three Infrared Atmospheric Sounding Interferometer (IASI) TIR Fourier Transform Spectrometer (FTS) instruments currently in orbit: IASI-A, B, and C onboard the Eumetsat satellites Metop-A, B and C, launched in 2006, 2012, and 2018, respectively. They fly in the same orbit, crossing the equator at ~9:30 a.m. LST. IASI observations comprise 4 pixels that each have a 12 km ground resolution at nadir. A 2200 km swath provides global coverage twice daily (Clerbaux et al., 2009). CO profiles are retrieved with the Fast Optimal Retrievals on Layers for IASI (FORLI, version 20151001) algorithm (Hurtmans et al., 2012), using invariant a priori information. IASI CO has been validated against ground-based observations (Kerzenmacher et al., 2012), aircraft data (Pommier et al., 2010; Klonecki et al., 2012) and other satellite measurements (George et al., 2009). Comparison between MOPITT and IASI CO records found that, while a priori was the dominant source of between-instrument bias, timing and vertical sensitivity differences also contribute to CO differences (George et al., 2015). While the IASI-A record is long enough to determine trends, it is worth noting that this CO record is not currently retrieved using homogeneous temperature, humidity and cloud information. This causes a few discontinuities in the IASI-A CO record, which could affect the long-term trend and it is therefore not suited for trend studies at this time. Different versions of these IASI auxiliary parameters (distributed by Eumetsat) have been improved over time (from V5 to V6 in Sept. 2014, and from V6 to V6.1 in Sept. 2015). Reprocessing of these data with homogeneous auxiliary data is in progress at Eumetsat but they are not yet available at the time of this analysis (Oct. 2019). Despite this, IASI data are still useful for confirming the hemispheric CO seasonality and interannual variability observed by the other satellites. NH and SH monthly average values for daytime (SZA < 80), were computed after filtering for Super Quality Flag (SQF) = 0 (see https://iasi.aeris-data.fr/CO_readme/), CO total column $< 20 \times 10^{18}$ molecules/cm^2, Root Mean Square (RMS) $\leq 2.7e^{-9}$ W/(cm^2 sr cm^{-1}) and $-0.15e^{-9} \leq$ bias $\leq 0.25e^{-9}$ W/(cm^2 sr cm^{-1}).

2.2.3. TES

The Tropospheric Emission Spectrometer (TES) was launched on the NASA/Aura satellite in 2004 and crosses the equator at 13:40 LST, 25 minutes after the NASA/Aqua satellite. TES measures radiance spectra of Earth's surface and atmosphere, with relatively fine spectral resolution (0.10 cm^{-1} at nadir, apodized) (Beer, 2006), and retrieves trace gases, temperature (Bowman et al., 2006) as well as cloud top pressure and cloud optical depth (Kulawik et al., 2006). TES CO profiles and total column amounts have been validated with respect to in situ measurements (Luo et al., 2007, 2015).

For this study, we use V007 Level 2 data and select daytime retrievals filtered with master quality flag = 1 (good) that accounts for variations

Table 1
Data selection criteria and specifications by instrument.

	MOPITT	AIRS	TES	IASI-A and IASI-B	CrIS
Instrument type	Gas filter correlation radiometer (GFCR)	Grating spectrometer	Fourier Transform Spectrometer (FTS)	FTS	FTS
Spectral range and resolution for CO	2140–2192 cm^{-1} (0.04 cm^{-1} effective)	2170–2200 cm^{-1} (~1.8 cm^{-1})	2086.06–2176.66 cm^{-1} (0.1 cm^{-1} apodized)	2143–2181.25 cm^{-1} (0.5 cm^{-1} apodized)	2185.25–2200 cm^{-1} unapodized (0.625 cm^{-1})
Data version	V8T (TIR-only)	V006	V007 Lite	FORLI 20151001	MUSES
Cloud screening	Clear sky conditions from MODIS Collection 6.1 and MOPITT Signal	Cloud-cleared radiances	Eff. cloud OD < 0.4	<25% clouds in pixel	Cloud effective optical depth < 0.1
Data quality	5A SNR > 1000; Remove Pixel #3; Retrieval Anomaly Diagnostics OK	QF = 0	Master QF = 1; DFS > 0.9	SQF = 0; COTC < 20×10^{18} molec./cm^2; RMS ≤ $2.7e^{-9}$ W/(cm^2 sr cm^{-1});$-0.15e^{-9}$ ≤ bias ≤$0.25e^{-9}$ W/(cm^2 sr cm^{-1})	Master QF = 1
Ground resolution	22 × 22 km	50 km x 50 km	8 × 5 km	12 km diameter	14 km radius
Daytime Global coverage	~3 days	Daily	Sparse sampling; 16 day orbit track repeat	Daily	Daily (sub-sampled in this study)
Column uncertainty for single obs.	5–6 %	10 %	6–7 %	A & B: 5–7 %	10-12%
Time range used	03/2000–12/2018	09/2002–12/2018	01/2005–12/2009	A: 01/2008–12/2018 B: 01/2013–12/2018	11/2015–3/2019
Instr. operation gaps	8–9/2009	20160924	4–6/2005 1–3/2010	none	5/2019
Avg. ret. per month	NH: 684520 SH: 627344	NH: 1419165 SH: 1359028	NH: 6249 SH: 3672	NH: A-2216361, B-2417436 SH: A-1905719, B-1976112	NH: 13071 SH: 12293
Data source	doi:10.5067/TERRA/MOPITT/MOP02T_L2.008	doi:10.5067/Aqua/AIRS/DATA202	NASA Langley Atmospheric Science Data Center. doi:10.5067/AURA/TES/TL2COLN.007	A: doi:10.25326/16 B: doi:10.25326/17	JPL MUSES team (tes.jpl.nasa.gov)

in retrieval performance, e.g., residual radiance mismatch, and the degrees of freedom for signal (DFS)⩾0.9. The TES algorithm retrieves on both clear and cloudy scenes, but for this work, only clear scenes are considered in month averages. Cloud-free retrieval criteria are defined as an effective cloud optical depth (OD)⩽0.4. Prior to December 2005, the TES instrument was in a different configuration for CO (Rinsland et al., 2006), resulting in a land bias for filtered data, especially over the fire-prone regions of South America and Africa. After 2005, sampling footprints are nearly uniformly distributed over land and ocean when filtered. Consequently, we use TES data after December 2005. Also, in order to conserve the instrument lifetime, from 2010 onwards routine sampling was spatially limited. Therefore, TES data acquired after 2009 are not included in our analysis.

2.2.4. CrIS

The Cross-track Infrared Sounder (CrIS) was launched in October 2011 on the Suomi National Polar-Orbiting Partnership (S-NPP) satellite (NOAA-19) with an equator-crossing time of ~13:30 LST. The CrIS scan pattern consists of nine detectors (each called a Field of View: FOV) in a 3×3 pattern (collectively named a Field of Regard: FOR). At nadir, each FOV diameter is ~14 km. The CrIS cross-track scan consists of thirty Earth-view FORs, plus additional calibration FORs. CrIS is a FTS operating in three spectral bands between 648 cm^{-1} and 2555 cm^{-1}, including the CO TIR R-branch above 2155 cm^{-1}. CrIS achieves daily coverage of over 95% of Earth's surface. The full-spectral-resolution retrieval of CO (0.625 cm^{-1}) has been operational since late 2015, with significant improvements in sensitivity to CO compared to the original 2.5 cm^{-1} resolution (Gambacorta et al., 2014). Here we use CrIS retrievals processed by the MUlti-SpEctra, MUlti-SpEcies, MUlti-SEnsors (MUSES) algorithm (Fu et al., 2016), which performs single pixel (FOV) retrievals, and has heritage in the TES algorithm (e.g.,Worden et al., 2007; Luo et al., 2013), using the same Kulawik et al. (2006) approach for retrievals of cloud. Retrievals presented here use the NASA v2 L1B Full Spectral Resolution (FSR) radiances (Revercomb and Strow, 2018), which are available from November 2015 onward. CO retrievals from FSR radiances offer significant improvements in sensitivity compared to retrievals using the nominal spectral resolution (NSR) radiances (δ = 2.5 cm^{-1} in the CO region) (Gambacorta et al., 2014).

In order to expedite analysis, sub-sampling of observations was tested to ensure that the NH and SH CrIS monthly averages were insensitive to the sub-sampling employed (Appendix A1.2). Like TES, the MUSES algorithm retrieves in all-sky conditions. Cloud-screening was performed, using an effective cloud optical threshold of 0.1. While there are operational CrIS CO products available for the FOR from NUCAPS (NOAA Unique Combined Atmospheric Processing System, Gambacorta, 2013), we instead use the MUSES single pixel (FOV) retrievals to take advantage of the full CrIS CO spatial resolution and error characterization derived from optimal estimation.

2.3. Trend analysis methodology

In order to compare total column CO timeseries from different satellite instruments, we convert to column average VMR (X_{CO}) by dividing by the reported dry air column for each retrieval. Trends are reported as relative trends (% per year) by dividing by the dataset mean value. Relative trends in XCO are equivalent to relative trends in total column CO, but using X_{CO} removes the dependence on surface topography that varies for the different instruments with different horizontal footprints.

The first step in trend determination is to remove the seasonal variability, which can obscure any linear trend. For the global map plots of column CO and AOD trends (Section 3.2), we remove seasonal variations using a 12-month running average prior to computing the linear trend. The endpoints are truncated, effectively removing the first and last 6 months for all the time series. This determines our bounds for the long-term trend as July 2002 - June 2018. For hemispheric and regional time series analysis (Section 3.3. and 3.4), we remove the seasonal variations in X_{CO} and AOD by subtracting the dataset mean annual cycle (with monthly resolution) to produce an anomaly time series.

Trend analysis on deseasonalized data proceeds by calculating the slope of a line for the linear equation:

$$y = mt + b + \varepsilon(t) \quad (1)$$

where y is the dependent variable (e.g. CO amounts), t is time in

fractional years, m is the slope (or linear trend), b is a constant and $\epsilon(t)$ is the noise, or residual. Weighted Least Squares (WLS) linear regression, weighted by the monthly variance, is used to calculate hemispheric and regional trends by estimating the linear slope via equation 2:

$$m = \frac{\sum_{i=1}^{n}\frac{1}{\sigma_i^2}\sum_{i=1}^{n}\frac{t_i y_i}{\sigma_i^2} - \sum_{i=1}^{n}\frac{t_i}{\sigma_i^2}\sum_{i=1}^{n}\frac{y_i}{\sigma_i^2}}{\sum_{i=1}^{n}\frac{1}{\sigma_i^2}\sum_{i=1}^{n}\frac{t_i^2}{\sigma_i^2} - \left(\sum_{i=1}^{n}\frac{t_i}{\sigma_i^2}\right)^2} \quad (2)$$

for y_i (e.g. CO month average values) with σ_i standard deviation associated with time t_i, where n is the total number of data points. Standard error in the slope (σ_m) is calculated two ways: using the WLS calculations or creating an estimate that compensates for first-order autocorrelation in the noise (Appendix A3, Weatherhead et al., 1998). The greater of the two error values is recorded as a conservative estimate of the standard error in the slope. A significant trend is defined as being outside one standard error.

Monthly statistics in MOPITT CO are determined by collecting all X_{CO} within a region (filtered as described in Section 2.1.1) for a particular month and year followed by calculations of the mean, standard deviation, median, 25th and 75th percentiles. The Theil-Sen method (Theil, 1950; Sen, 1968) is used to analyze the long-term trends in X_{CO} percentiles separated by month for each region (Section 4.2). Theil-Sen analysis is a non-parametric trend estimation technique that calculates all the slopes between pairs of points and takes the median of these slopes (Eq. (3)):

$$m = \left(\widetilde{\frac{y_j - y_i}{t_j - t_i}}\right) \quad (3)$$

for all y_j, y_i dependent variable values associated with the t_j, t_i times, for $j > i$. Significance of a Theil-Sen trend is determined using the Mann-Kendall test for p values < 0.05, 0.01 and 0.001 (Mann, 1945; Kendall, 1975). We show in Appendix B1 that Theil-Sen results for the whole time series are consistent with the WLS method. Note that because the lifetime of CO is ~2 months and consecutive values are a year apart the autocorrelation is not significant and is not considered for trends calculated by month (Appendix A3).

A full description of the uncertainty analysis on the X_{CO} trend calculations is provided in Appendix A. Systematic sampling uncertainty is approximated by performing trend analysis on a priori (Appendix A1.1) and random sampling uncertainty by using bootstrap analysis (Appendix A1.2). Systematic uncertainty from changes in instrument sensitivity over the MOPITT record is explored using averaging kernels applied to a reanalysis climatology (Appendix A2). Autocorrelation is analyzed for each region (Appendix A3). We also assess the consistency between trend determination methods (Appendix B1) as well as the robustness of the trend to removing the influence of outliers such as the large El Niño fires in 2015 (Appendix B2).

3. Results

3.1. Zonal average time series of CO and AOD

We show the latitudinal and seasonal dependence of column CO and AOD using the zonal average time record (Fig. 1a and b). The annual cycle of CO (Supplementary Fig. C3) is determined by a combination of source seasonality and removal by reaction with OH. Photochemically produced OH depends on incoming solar radiation, leading to lower reactivity in winter and higher reactivity in summer. In the background atmosphere, the OH sink dominates the seasonal behavior of CO. Consequently, the build-up of CO over the winter months produces an early spring peak, and destruction during summer leads to a late summer minimum. Since removal of aerosols is mainly by dry and wet deposition (e.g., Kanakidou et al., 2005), there is no corresponding winter accumulation, and AOD seasonality is determined mainly by production processes. Production by photochemical oxidation again depends on OH availability, and peaks in summer for secondary aerosol types such as sulfate aerosols (e.g., Edwards et al., 2004) and secondary organic aerosols (SOA) (e.g., Lack et al., 2004). Direct fire emissions of carbonaceous aerosols follow the annual cycles of dry season burning.

Due to pollution sources, both CO and AOD show higher mean values in the Northern Hemisphere (NH) compared to the Southern Hemisphere (SH). Peak CO at 30° to 50° N occurs at higher latitudes than the peak AOD (15° to 25° N). Enhanced CO columns are mainly influenced by fire and anthropogenic emissions, while AOD additionally experiences strong contribution of dust at lower latitudes that combines with the anthropogenic and fire aerosol sources. The lifetime of CO allows it to be transported to higher latitudes by dominant poleward flow, while aerosols with shorter lifetimes produce AOD enhancements closer to source regions. Peak NH AOD is shifted equatorward in this study when compared to Edwards et al. (2004), which is a result of including the Deep Blue AOD retrieval over dust source regions, such as the Sahara, Middle East, Gobi, Taklamakan and India deserts. This algorithm was not available in the Edwards et al. (2004) study which used MODIS Collection 4. Additionally, Levy et al. (2013) found that AOD in MODIS C6 is generally lower than Collection 5 for Europe and North America, but higher over Eastern Asia.

The SH peak and interannual variability for both CO and AOD in the tropics are mainly driven by biomass burning in South America, Africa, Maritime Southeast Asia (SEA) and Australia (Edwards et al., 2004; Edwards et al., 2006). The impact of CO and aerosol lifetime differences is also apparent as evidenced by the smearing of fire enhanced CO poleward (Fig. 1a) compared to AOD (Fig. 1b). The consistent feature of relatively large AOD at temperate southern latitudes (40° to 60° S, Fig. 1b) is due to maritime aerosols such as sea salt (e.g., Witek et al., 2016), ocean biogenics, or transported smoke.

The anomaly plots show the percent anomaly relative to the monthly means (Fig. 1c and d). In general, relative interannual variability for CO shows similar strength between hemispheres, while for AOD, the SH interannual variability appears weaker than the NH (less saturated colors). Several large anomalies are consistent between CO and AOD. For example, the 2003 high northern latitude enhancement is a response to the large boreal fires in Western Russia (e.g., Edwards et al., 2004). The large 2015 El Niño driven Maritime Southeast Asia (SEA) fire season emissions in September and October (Huijnen et al., 2016; Field et al., 2016) had a widespread impact, producing the CO and AOD positive anomalies at the end of 2015 and the beginning of 2016. These examples highlight the direct co-emission of CO and aerosol from fire events. In contrast, AOD includes many anomalies that are absent in the CO record, for example, the AOD anomaly in 2018 at about 20° N that was mainly due to dust emissions over the Arabian peninsula, combined with exported dust from the Sahara (Voss and Evan, 2020).

The large positive anomalies in Fig. 1c and d illustrate the substantial interannual variability in both the CO and AOD records. However, we can also see that the background CO shows an overall global downward trend as observed by more widespread cool colors in later years compared to earlier years. In contrast, AOD shows a general upward trend in the SH while the NH seems to increase between 2008 and 2012, followed by decrease. We investigate these trend behaviors in more depth in the following sections.

3.2. Spatial analysis of trends in CO and AOD

Fig. 2a and b show the 2000–2018 global average maps of CO and AOD, respectively. Regions of high values for both constituents are apparent over Northeast China, North India and Central Africa. Trends in CO and AOD from 2002–2018 are shown in Fig. 2c and d, globally gridded at 2°x4° (significance analysis in Appedix C, Figure C1). The overall decline in CO coincides with the improvements in combustion efficiency for anthropogenic sources (Zheng et al., 2018b), as well as the decrease in global fire emissions, e.g. from 1997 to 2009 as shown in the

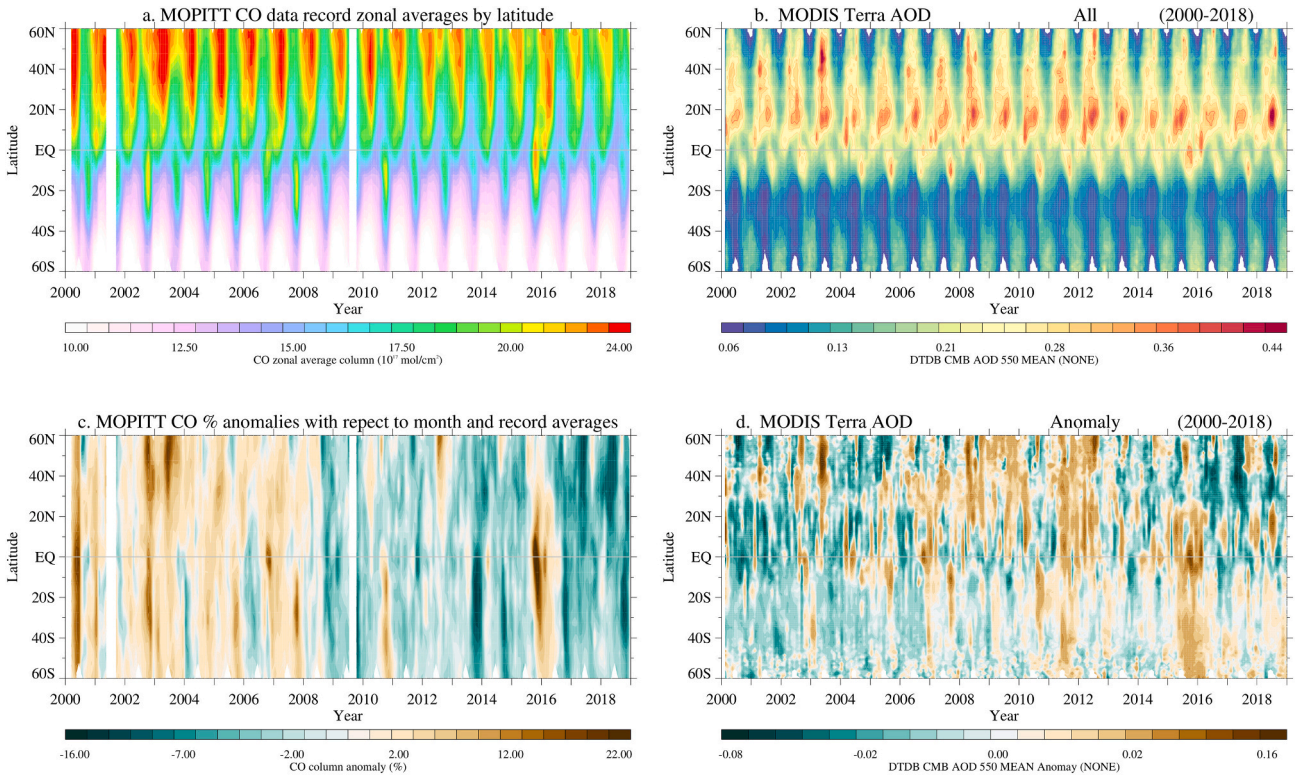

Fig. 1. Zonal average plot of monthly average (a) MOPITT column CO and (b) MODIS AOD. Percent anomalies in (c) MOPITT CO and (d) MODIS AOD. Percent anomalies are calculated relative to the climatological month averages within each 2° zonal average box. White stripes in panel a and c during 2001 and 2009 represent missing MOPITT data due to instrumental diagnostic operations. White pixels at NH and SH high latitudes represent missing data for both instruments due to polar night.

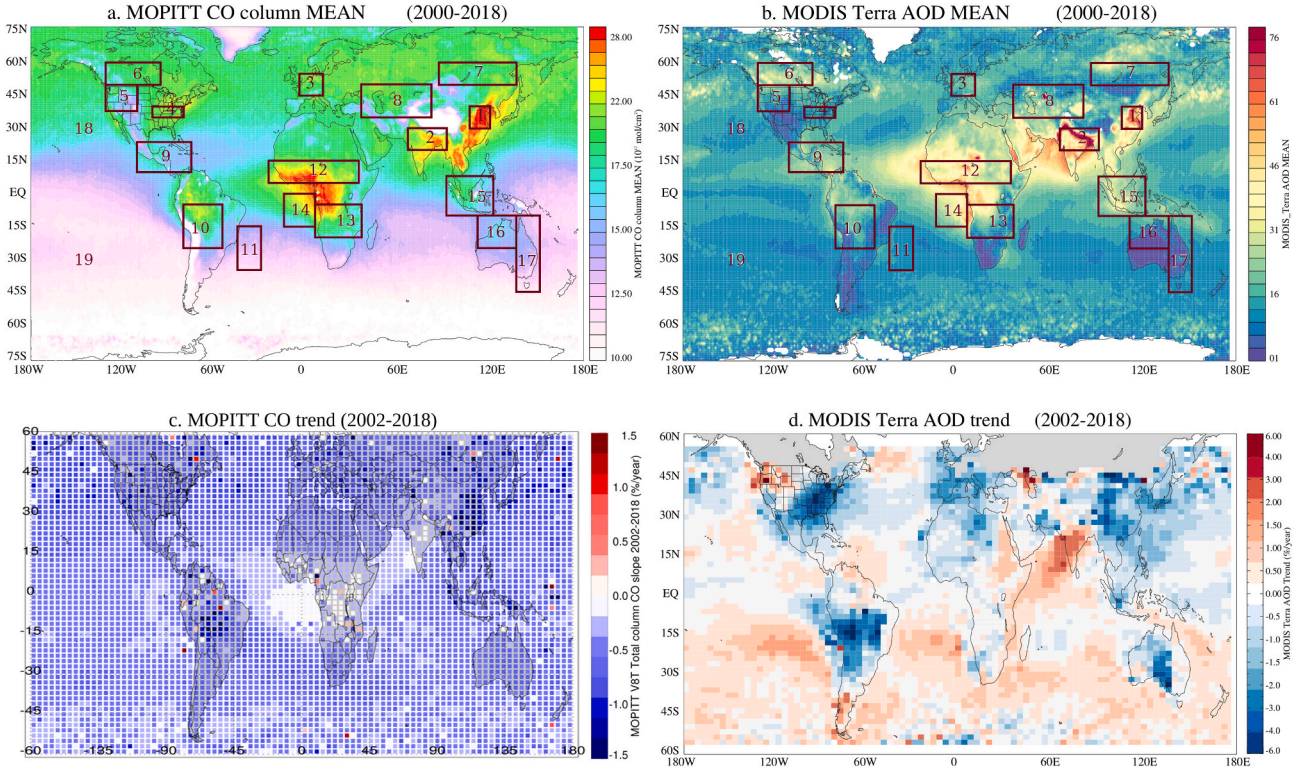

Fig. 2. Global average (a) column CO and (b) AOD between 2000 and 2018. Boxes outline the sub-regions used for regional trend analysis, numbered 1 to 19, discussed in Section 3.4 and listed in Table 2. Trends in (c) CO from MOPITT and (d) AOD from MODIS between 2002 and 2018, gridded to 2°x4°.

Global Fire Emissions Database, Version 3 (GFED3) inventory (van der Werf et al., 2010) and the negative trend in global burned area in Andela et al. (2017) from 1998 to 2015. Since fire emissions account for about 33% of global CO emissions (Yin et al., 2015), a trend in fires can have substantial effect on atmospheric CO. AOD trends are more regionally variable and reflect changes in the different sources.

Burning regions around the South Atlantic show different trend results (Fig. 2c and d). South America has seen a strong decrease in both CO and AOD over the whole record due to the long-term decrease in burning there (Andela et al., 2017; Deeter et al., 2018). However, recent increases in Amazon deforestation burning over the last few years may alter trends in that region, especially for the recent decade. In contrast, Central/Southern Africa shows no trends in CO and AOD. Increasing burning in this region (Andela et al., 2017) might be counteracting transported decreasing trends. In addition, Zheng et al. (2019) find an increasing trend in anthropogenic sources in Central Africa that could also counteract the global downward CO trend. The AOD trend may be further confounded by dust and anthropogenic variability. In comparison, the Pacific Northwest (PNW) has less interference from dust or anthropogenic aerosol sources and consequently sees a positive AOD trend due to climate driven changes in fire (McClure and Jaffe, 2018). The CO trend in the PNW is lower than the global average, but local behavior is combined with strong downward trends in transported CO from Asia. Therefore, CO is still decreasing in the PNW year to year.

To help interpret regional CO trends, we calculate CO residual trends. The lifetime of CO (~2 months) is such that a global mean trend can be detected in well-mixed background air. We find the global mean CO trend (±60° latitude) between 2002 and 2018 to be −0.50 (±0.3) % per year, which is a slow-down relative to the approximate −1 % per year trend between 2000 and 2011 found by Worden et al. (2013) using MOPITT V5 retrievals. This difference reflects an atmospheric response because both MOPITT versions saw negligible drift in column amounts from TIR retrievals (Deeter et al., 2013, 2019). The slow-down is potentially due to diminishing returns from improvements in combustion efficiency and emission controls, as has been suggested by McDonald et al. (2013). In addition, emissions from economic production and transport have returned to pre-recession levels following the 2008–2009 global economic crisis (e.g., de Ruyter de Wildt et al., 2012). The residual trend in CO was calculated by subtracting the global mean trend from the total trend within 2° by 4° gridboxes. The result is a map of residual trends that enables interpretation of local behavior relative to the global mean trend (Fig. 3) and reveals regions that are decreasing faster than the global average (blue colors), and regions that are decreasing slower than the global average trend (red colors), suggesting increasing regional emissions that counteract the global trend. Light colors show where the trend is close to the global average. A global average trend for AOD is not meaningful due to the shorter lifetime (~8 days) of aerosols, so we do not calculate residual AOD trend.

The different response in the two Atlantic fire-prone regions (South America and Central/Southern Africa) is immediately clear in the CO residual trend map. Residual trends from these regions extend into their respective outflow paths over the Atlantic Ocean. Different patterns are also clear for industrial regions. Northeast China experiences the most negative CO trends globally, resulting from rapid improvements in combustion efficiency and a recent focus on air quality control (Zheng et al., 2018a, 2018b; Tang et al., 2019). However, AOD decreases in Northeast China are weaker than in Eastern USA, reflecting the relatively new air quality policies in China compared to the longer-term focus in USA. India, on the other hand, shows strong increases in AOD and the CO residual trends are positive suggesting local pollution sources counteract any transported or background decreases in CO.

In the following sections we examine regional trends in more detail, including calculations of trend significance.

3.3. Hemispheric CO record across different instruments

Fig. 4 shows the hemispheric monthly mean X_{CO} time series from all satellite instruments (MOPITT, AIRS, TES, IASI-A/B and CrIS) available between January 2001 and December 2018. Overall, X_{CO} magnitude, seasonal patterns, and interannual variability are consistent between instruments. Some differences in X_{CO} values arise because we have not accounted for differences in sampling coverage, horizontal resolution or vertical sensitivity between instruments. Although column results are less sensitive than profile retrievals to differences in vertical sensitivity, the different averaging kernels between instruments could give rise to slightly different results when applied to the same atmospheric state (George et al., 2009, 2015). Comparisons of MOPITT, AIRS, TES, and IASI were previously conducted by George et al. (2009) and Warner et al. (2010), who found that biases are due to differences in spatial sampling, instrument spectral resolution and retrieval methodology,

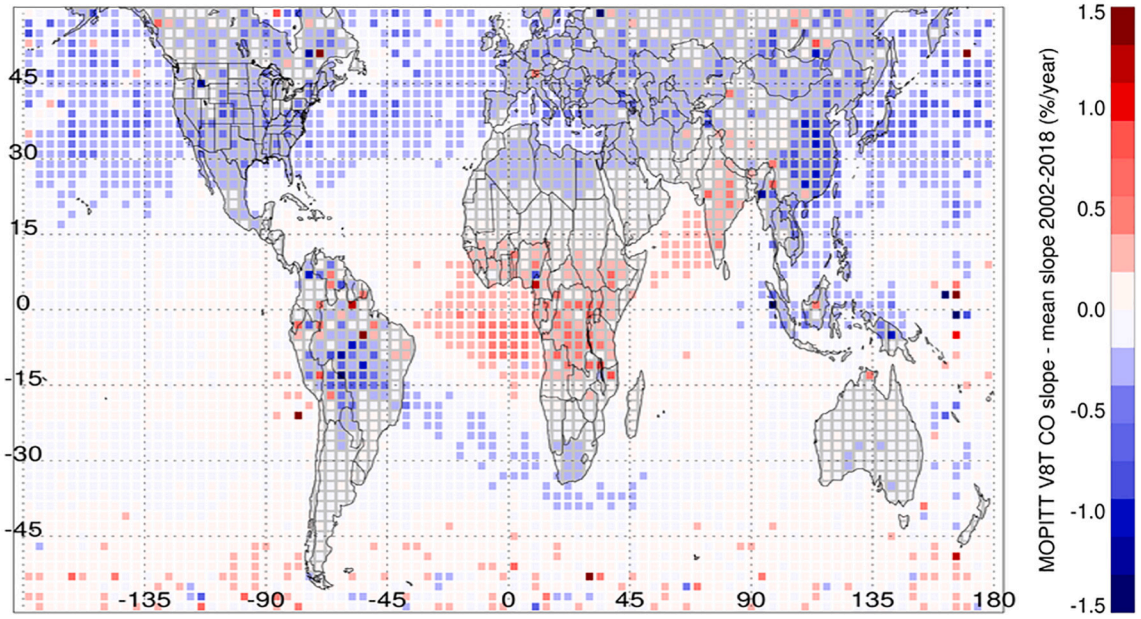

Fig. 3. Residual trend in CO columns from MOPITT calculated relative to the global average trend (−0.5% per year, +/- 60°) from 2002 to 2018.

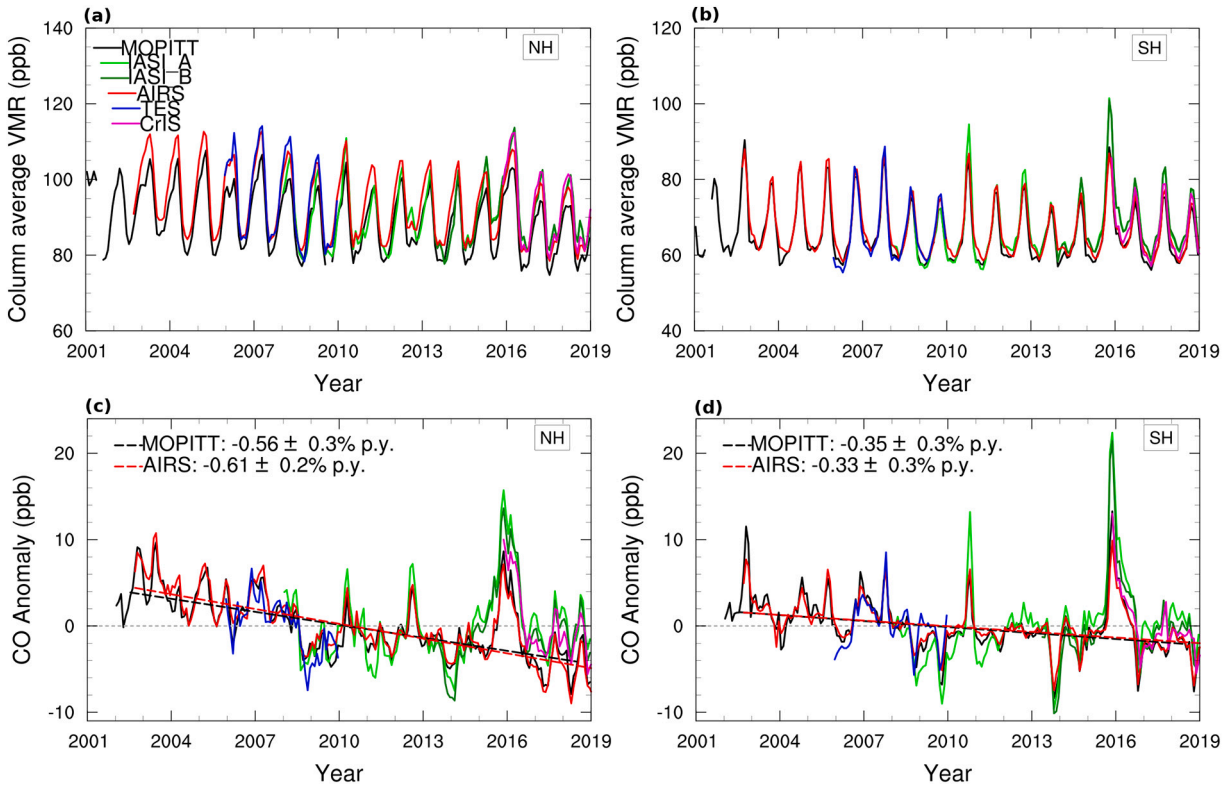

Fig. 4. Multi-instrument time series of month average X_{CO} for (a) NH (0° to 60°N) and (b) SH (60°S to 0°). Lower panels show the monthly anomalies relative to each dataset mean annual cycle, for (c) NH and (d) SH. Weighted least squares trends on the anomalies are indicated with standard error in percent per year for MOPITT and AIRS. The grey dashed line is the zero line for reference.

including different a priori information. Additionally, the number of TES observations is 2 orders of magnitude lower than the other instruments, so we expect the non-colocation of TES observations with other instrument footprints to contribute to the CO differences. The SH high bias previously found when using AIRS V5 (Warner et al., 2010; Worden et al., 2013) has been removed in the comparison using updated retrievals from both instruments.

Fig. 4c and d show the NH and SH anomaly records for all satellite instruments computed by subtracting the respective instrument record climatological monthly means. Anomalies reflect interannual variability due to changes in fire emissions that are in turn linked with climate variability (Buchholz et al., 2018), such as the 2015 El Niño influenced fire emissions from Maritime SEA (Huijnen et al., 2016) that impacted both hemispheres. There is also a relationship of lower X_{CO} with lower anthropogenic emissions due to the global financial crisis starting in late 2008, particularly for the NH (e.g., de Ruyter de Wildt et al., 2012).

Trend values from linear fits (July 2002-June 2018) are shown for MOPITT and AIRS in Fig. 4c and d, with standard errors. While IASI-A has a long enough record to determine trends, it currently does not have a fully harmonized record suited for trend analysis (see Section 2.2.2). The instruments with shorter time records, IASI-B, TES and CrIS, do not show significant trends. However, all instruments show similar variability, lending confidence to the use of MOPITT and AIRS records for trend determination. MOPITT and AIRS X_{CO} trends are consistent within $<1\sigma_m$. The SH trend is less negative than the NH trend, and both hemispheres have a reduced trend compared to Worden et al. (2013). Although it does have some impact, we find that the large emissions in 2015 are not the main reason for the CO trend slow down (Appendix B2).

3.4. Regional trends in CO and AOD

In addition to hemispheric trend analysis, we select a number of regions for more detailed consideration (Fig. 2a). Four industrial regions were chosen to align with Worden et al. (2013): Northeast China, North India, Europe and Eastern United States. Other regions are selected based on the residual trend patterns from Fig. 2, combined with the burned area trends in Andela et al., 2017. Due to the shorter lifetime of aerosols, it was not relevant to calculate hemispheric trends for AOD, so only regional trends are shown.

CO trends (in X_{CO}) and AOD trends, determined for the different subregions are shown in Table 2, for the full 16-year period (July 2002-June 2018), as well as for two 8-year sub-periods (1st half: July 2002-June 2010 and 2nd half: July 2010-June 2018). CO trends in the first half of the record are consistent with those found in Worden et al. (2013). Significant negative CO trends in the 1st half of the record shift to slower, non-significant trends in the 2nd half. This leads to an overall slowdown in the CO downward trends for the full time period in every region. Exceptions are Southern Africa and South America, which show no significant CO trend for any time period. This is consistent with Strode and Pawson (2013) who found more than 20 years of data are necessary to find CO trends over highly variable regions. AOD is more regionally variable and generally shows more positive AOD trends in the 1st half of the record compared to the 2nd half.

Northeast China has the strongest negative CO trend across all time periods, at more than −1% per year. AOD in China moves from a positive to negative trend between first and second halves of the record, coinciding with the clean air policy implementation in 2010. The CO trend in India is substantially lower than the other industrial regions and the full time period shows a significant positive trend in AOD, reflecting the minimal emission controls in that region. While in the first half of the record, both Europe and Eastern USA CO are decreasing at similar rates, in the second half, the Eastern USA CO trend is stronger than in Europe. This may be due to stronger local focus on air quality improvements in the USA than in Europe, as supported by the coinciding large downward trend in Eastern USA AOD and the stronger reductions in USA

Table 2
Summary of Weighted Least Square (WLS, Eq. (2)) trends in CO (X_{CO}) and AOD for the monthly anomaly values over different time periods for 19 regions.

	Trend % per year (± standard error + systematic error)					
	CO			AOD		
	Full July 2002-June 2018	1st half July 2002-June 2010	2nd half July 2010-June 2018	Full July 2002-June 2018	1st half July 2002-June 2010	2nd half July 2010-June 2018
Industrial						
1. NE China	-1.18 (0.3-0.1)	-1.94 (0.8)	-1.02 (0.7)	-0.97 (0.5)	1.70 (1.5)	-5.15 (1.5)
2. N India	-0.28 (0.2)	-0.56 (0.5)	-0.17 (0.5)	1.34 (0.7)	1.45 (1.9)	1.50 (2.2)
3. Europe	-0.89 (0.1+0.05)	-1.58 (0.3)	-0.47 (0.3)	-0.97 (0.4)	0.26 (1.2)	-1.51 (1.1)
4. E USA	-0.85 (0.1+0.03)	-1.59 (0.3)	-0.73 (0.4[a])	-2.06 (0.3)	-0.89 (1.7[a])	-3.84 (1.5[a])
Fire-prone						
5. NW USA	-0.85 (0.2+0.1)	-1.44 (0.5+0.1)	-0.67 (0.4)	0.26 (0.6)	2.85 (1.7)	-0.19 (2.7[a])
6. NW Canada	-0.60 (0.1+0.04)	-1.35 (0.4[a]+0.05)	-0.51 (0.3+0.03)	-1.63 (0.3)	-4.21 (1.0)	-4.74 (1.2)
7. Siberia	-0.59 (0.2[a])	-1.34 (0.6[a]-0.03)	-0.32 (0.4-0.03)	0.78 (1.0[a])	2.47 (3.6[a])	-2.51 (1.2)
8. Russia	-0.80 (0.1+0.1)	-1.38 (0.4+0.1)	-0.66 (0.3+0.1)	0.90 (0.9)	2.23 (2.3)	-3.35 (3.3)
9. Central America	-0.46 (0.1)	-1.05 (0.4)	-0.23 (0.4)	0.18 (0.4)	0.12 (1.1)	-0.03 (1.1)
10. S America	-0.31 (0.4[a])	-0.47 (1.0[a])	0.02 (1.0[a])	-0.43 (1.3[a])	-2.18 (3.7[a])	1.22 (3.2[a])
11. SAm Transport	-0.39 (0.2)	-0.77 (0.5)	-0.03 (0.8[a])	0.59 (0.3)	1.11 (0.7)	0.16 (0.8[a])
12. Central Africa	-0.22 (0.2)	-0.55 (0.5)	-0.12 (0.5)	-0.10 (0.5)	0.06 (1.4)	0.92 (1.4)
13. Southern Africa	-0.17 (0.3)	-0.63 (0.7)	-0.09 (0.7)	-0.12 (0.6)	-0.79 (1.8)	-0.77 (1.8)
14. SAf Transport	-0.07 (0.2)	-0.46 (0.6)	0.14 (0.6)	0.16 (0.4)	-0.30 (1.2)	-0.72 (1.1)
15. Maritime SEA	-0.51 (0.4[a]-0.1)	-1.08 (1.0[a]-0.2)	-0.14 (1.3[a])	-0.29 (1.0[a])	-0.73 (2.3[a])	0.07 (3.4[a])
16. NW Australia	-0.25 (0.3[a])	-0.79 (0.7[a])	0.03 (0.7[a])	0.31 (1.0)	1.23 (2.8)	-0.88 (3.1)
17. E Australia	-0.32 (0.2)	-0.90 (0.5)	0.16 (0.6[a])	0.47 (0.8)	1.02 (2.2)	-0.56 (2.5)
Background						
18. NH (0 to 60)	-0.57 (0.3)	-1.12 (0.9)	-0.43 (0.8)	Inconclusive due to land/ocean and mix of regions		
19. SH (-60 to 0)	-0.35 (0.3)	-0.9 (1)	-0.1 (1)			

Standard error in the slopes are also shown in brackets. Systematic error is also shown where it was found to be significant (Appendix A). Colors define the trend type, determined significant relative to one standard error. Red background colors denote positive trends, blue denotes negative trends and yellow denotes no significant trend. Region numbers correspond with regions in Fig. 2.

Cardinal directions are abbreviated (e.g. Northeast = NE); SAm = South America, SAf = Southern Africa, SEA = Southeast Asia.
[a]Standard error is taken from the estimate including autocorrelation where it is larger than the WLS estimate (Appendix A3).

anthropogenic CO emissions since 2010 compared to Europe as found by Jiang et al. (2017). Additionally, Eastern USA may be more influenced by CO transport from China than Europe, and consequently reflects the negative trend in transported CO.

4. Discussion

4.1. Covariation of CO and AOD

Co-variability analysis of CO and AOD provides further insights into trend behavior. Cloud masking may contribute to some monthly variability, but quantifying this contribution is beyond the scope of this study. However, we expect the main source of seasonal variability to be driven by chemical and physical processes, as discussed in Section 3.1. Additionally, because both MOPITT and MODIS use the MODIS cloud detection, differences between their variability is expected to be due to source or chemistry differences. Co-variability in the industrial regions, (Fig. 5 and annual cycles in Supplementary Fig. C3), ranges from little correlation between peak CO and peak AOD (e.g. North India) to a strong relationship (e.g. Northeast China).

In Northeast China (Fig. 5a, Supplementary Fig. C3), both CO and AOD peak in late spring/early summer, but AOD remains high while CO rapidly decreases. This reflects the opposite effects of OH photochemistry on CO and sulfate aerosols, as well as the impact of dust aerosols on AOD during the dry summer months (Luo et al., 2014; Proestakis et al., 2018). The residential, industrial, and transportation sectors dominate CO emissions in China (Streets et al., 2006; Li et al., 2017). Residential CO emissions include biomass and coal burning (Wang and Hao, 2012) and are generally higher in winter and spring than in summer (Liu et al., 2016). In addition, agricultural burning usually peaks in June in this region (Wu et al., 2017; Li et al., 2018) and may also contribute to high CO in June. The decline in Northeast China CO during the first half of the record does not correspond with a decline in AOD. This reflects the move to centralized energy production that improved combustion efficiency by replacing residential coal use with electricity and natural gas. This change in energy production had relatively large impacts on emissions of CO, but not on aerosols. In 2010, China implemented Clean Air Policies (van der A et al., 2017; Zheng et al., 2018a) and as a result, AOD started decreasing along with the continued decrease in CO, as seen at the inflection point around 2010 in Fig. 5a. This inflection point is consistent with results found by Filonchyk et al. (2019) for the whole of China using MODIS and MISR. The AOD decrease past 2010 is also consistent with reductions in anthropogenically emitted aerosol precursors SO_2 and NO_2 since 2012 (Krotkov et al., 2016; Qu et al., 2019; Wang and Wang, 2020).

Over North India, CO and AOD variability are out of phase (Fig. 5b, Supplementary Fig. C3) with CO peaking in early spring and AOD peaking in summer. The spring peak in North India CO is related to the peak biomass burning activity (Bhardwaj et al., 2016). In India, mineral dust makes a large contribution to total AOD during the pre-monsoon season (Apr-Jun) while at other times of the year anthropogenic fine-mode aerosols are optically dominant (Sayer et al., 2014). A significant positive trend in AOD over the full time period (Table 2) is due to several anthropogenic factors including increased SO_2 and NO_2 emissions from coal-powered power plants (Krotkov et al., 2016; Li et al., 2017; Qu et al., 2019; Wang and Wang, 2020), more frequent fog events near the Indo-Gangetic Plain (Ghude et al., 2017), increased vehicular emissions (Manoj et al., 2019), and increasing crop-residue burning activity (Jethva et al., 2019). This region also shows the least negative CO trend, suggesting local emissions are offsetting the decreases in the global CO background. India's CO emissions were increasing from 1996–2015 mainly due to increases in residential and agricultural sources (Pandey et al., 2014) as well as due to power production and transport activities (Sadavarte and Venkataraman, 2014).

In both Europe and Eastern USA, the peak CO occurs before the peak AOD (Fig. 5c and d, Supplementary Fig. C3). This offset of several months is due to OH oxidation mainly driving seasonality, which maximizes in summer to remove CO and concurrently produce aerosol (Section 3.1). Both regions also show concomitant reductions in AOD and CO for the whole time period, reflecting the implementation of strong air quality and climate-related policies, as has been observed by reductions in anthropogenically emitted aerosol precursors SO_2 and NO_2 (Krotkov et al., 2016). Additionally, CO and AOD seasonal variability in both these regions appear larger in the 1st half than the 2nd half of the record, suggesting reductions in the peak emission months and potential impacts on the chemical oxidation environment.

Fire-prone regions often experience strong correlation between CO and AOD (Fig. 6a, Supplementary Fig. C3). The longer lifetime of CO is also clear in these regions, as observed by the peak AOD diminishing faster than CO, for example over Maritime SEA (Fig. 6a). Over northwest USA in the first half of the record, the CO seasonal cycle is dominated by a single spring-time peak (Fig. 6b). A significant secondary CO peak shows up in late summer in the second half of the record, and in some years is as large as the spring-time peak CO, for example in 2017 and 2018. This secondary CO peak coincides with a strengthening of the aerosol peak from about 2012 onwards. This pattern suggests a regime shift associated with increasing fire in the region. Similar patterns are seen for the Canada and Siberia fire-prone regions (not shown).

4.2. Separating CO trends by monthly percentiles

Trend analysis separated by month is used to determine the seasonal implications and potential sources of the long-term trend. Trends are calculated on the monthly means and percentiles (25th, median, 75th) between January, 2002, and December, 2018. Theil-Sen is used for trend calculation to minimize the impact of outliers.

Resulting trend arrays show a range of information useful for interpreting trends (Figs. 7, 8 and Appendix C, Figure C4). The size of the circle relates to the trend significance, with larger circles indicating adherence to a higher significance level. The color of the circles denotes the strength of the trend, with darker blues indicating stronger negative trends. The climatological annual cycle of column average VMR is displayed in colored squares on the left-hand side of the graph, where the size of the square represents the coefficient of variation - a larger square corresponds to higher variability. Finally, the mean number of monthly retrievals are indicated on the right-hand side of the plot.

It is apparent from the trend arrays which months and percentiles have strong and weak trends. Northeast China (Fig. 7a), experiences the strongest negative trends when compared to all other regions. Spring months (March, May and June) in Northeast China experience the strongest trends overall, at over −1.5 % per year for most of the percentiles in these months, which is consistent with the trend results found by Zhang et al. (2020). The downward trend is likely to be strongest in spring because the impact of residential emissions of CO is greatest during this season. The downward trend in Northeast China CO is also stronger in the 75th percentile compared to the 25th percentile, suggesting the trend is driven by a reduction in highly polluted events that would likely result from local sources.

Eastern USA (Fig. 7c) and Europe (Appendix C), also see stronger trends in the 75th vs. the 25th percentile, albeit smaller in magnitude

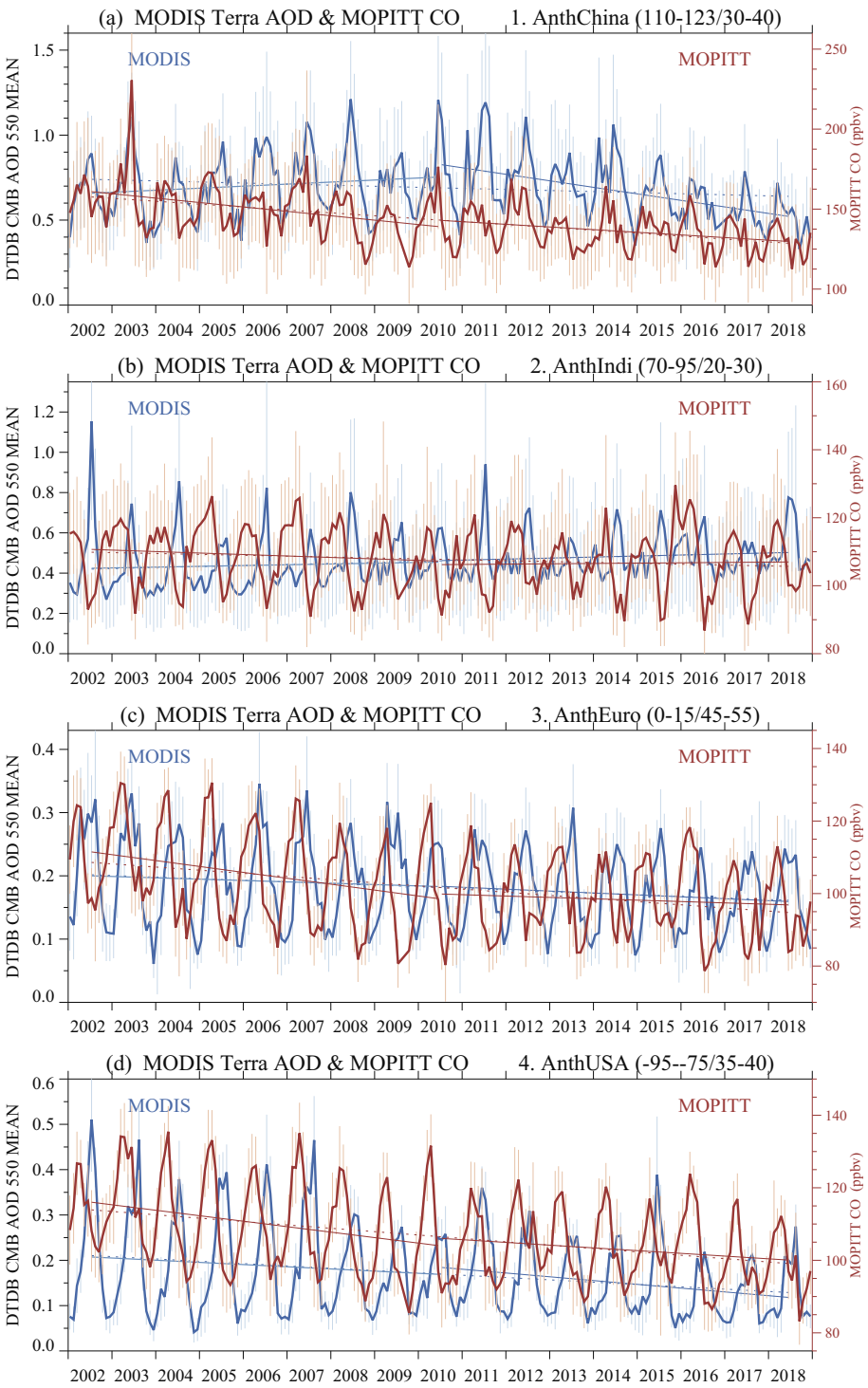

Fig. 5. Regional time series of month average X_{CO} (red) and AOD (blue) over industrial regions, Region numbers correspond with numbers in Table 2 and Fig. 2. Vertical bars are monthly standard deviation. General tendencies from linear regression (WLS) are shown for the whole record (July 2002-June 2018, dotted line), as well as the 1st half and 2nd half of the record (solid lines). Slope values are described in Table 2. (For interpretation of the references to colour in this figure legend, the reader is referred to the web version of this article.)

compared to Northeast China, implicating local emission reductions. In contrast, the trend array for North India (Appendix C) shows few significant trends, reflecting that high variability or a positive trend locally counteracts any reductions in transported CO. Where they are significant, trends occur more frequently in the 25th percentile for North India, representing a trend in background CO.

Many regions of the NH do not see significant trends in late summer and early autumn, i.e. August and September (e.g. Fig. 7). This leads to small trends with low significance for the whole NH during these months (Fig. 8a). Several factors may be influencing the CO trend in these months. The large summer sink may effectively process any sources independent of their magnitude, smoothing out any trend behavior. Additionally, variability is relatively large in these months (see c.v. for Northeast China and Northwest USA in Fig. 7a and c, respectively), which impacts the determination of significant trends. Finally, the recent upward trend in peak CO for boreal fire-prone regions described in Section 4.1 (e.g. Fig. 6b) likely counteracts the global downward trend. Fire emissions in these boreal regions impact not only the local atmosphere, but also downwind regions through atmospheric transport, and may be responsible for a hemispheric weakening of the CO trend in these months. A modeling study would be required to quantify the contributions of each of these processes to trend determination.

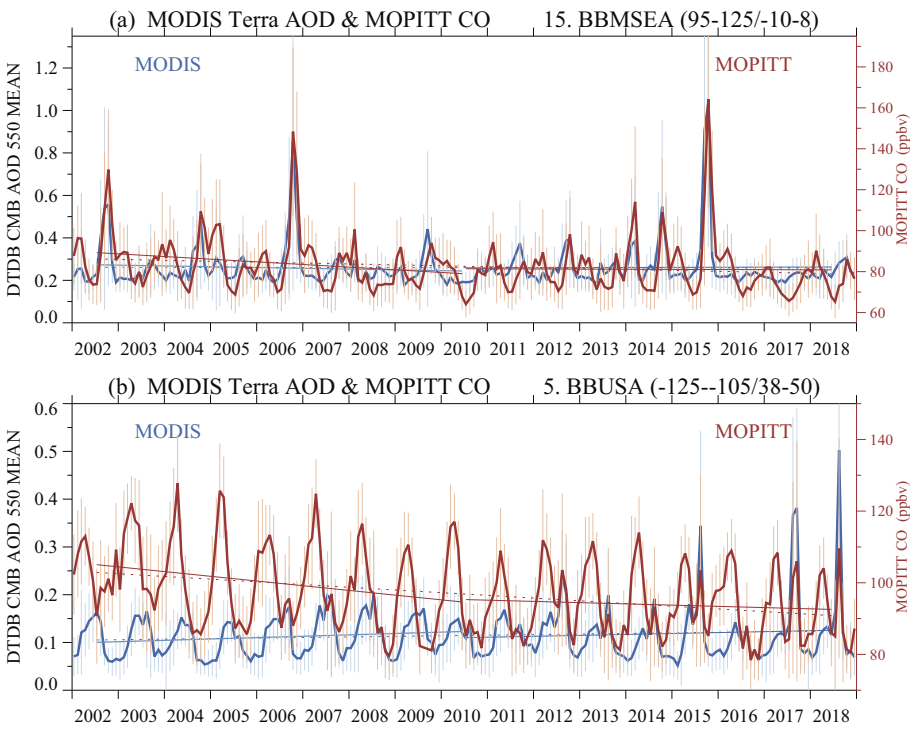

Fig. 6. Regional time series of X_{CO} (red) and AOD (blue) over (a) Maritime Southeast Asia and (b) the northwest USA example fire-prone regions. Vertical bars are monthly standard deviation. General tendencies from linear regression (WLS) are shown for July 2002-June 2018 (dotted line), as well as the 1st and 2nd half of the record (solid lines). Slope values are described in Table 2. (For interpretation of the references to colour in this figure legend, the reader is referred to the web version of this article.)

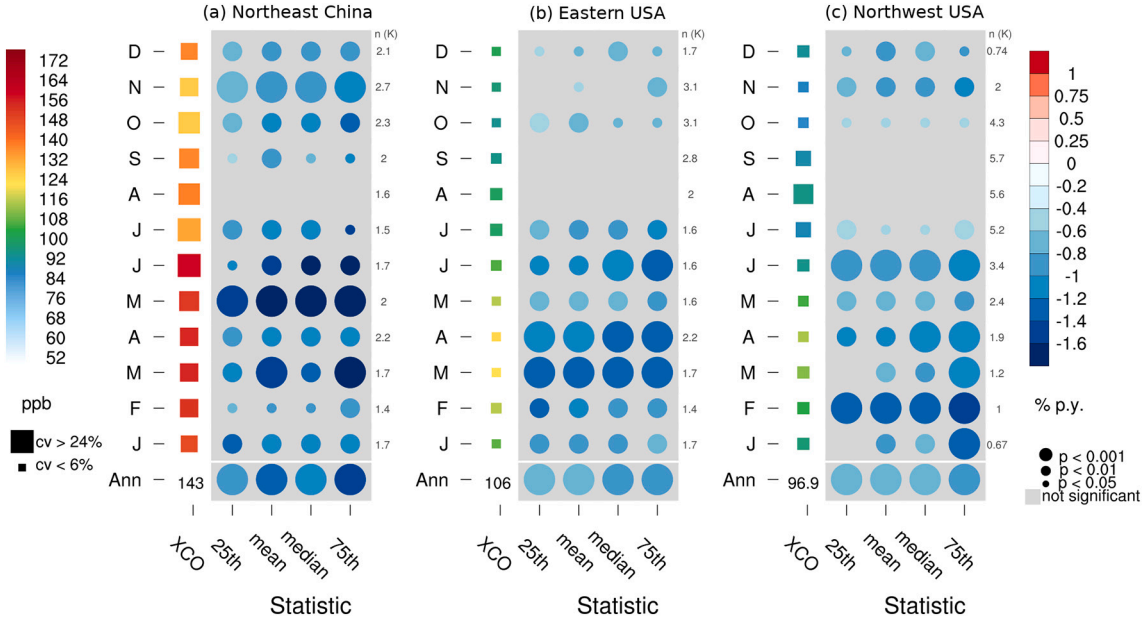

Fig. 7. Arrays of quantile trend analysis for monthly CO data for different regions: (a) Northeast China, (b) Eastern USA, and (c) Northwest USA. Trends are shown as circles colored by percent per year, which is calculated relative to the regional mean column average VMR, noted in the bottom left. The Mann-Kendall p-value associated with Theil-Sen trend analaysis is indicated by the size of the circle. Trends by month for January to December travel up the page, and trends on annual average values are shown in the bottom row for comparison. Month average column average VMR is displayed as colored squares on the LHS with size of the square denoting coefficient of variation (σ/μ). The mean number of retrievals (n) within a month are displayed on the RHS, in amounts of thousands (K).

While the NH shows negative trends across all months of the year, the SH trends are more confined to one season. The SH sees no significant trends in mid-summer to early autumn (January to April, Fig. 8b), suggesting that sources are in equilibrium with the photochemical sink at this time of year. The downward CO trend is dominant in the fire season (Aug-Nov), which is consistent with the Andela et al. (2017) global decrease in burned area, and considering biomass burning is the major source of CO emissions in the SH (Holloway et al., 2000). Small CO trends prior to the SH burning season (May-July) may be due to a trend in transported air from the NH (Zeng et al., 2012; Yang et al., 2019). Overall, the SH trend is mainly determined by the trend from fires, while the NH trend also includes improvements in combustion efficiency.

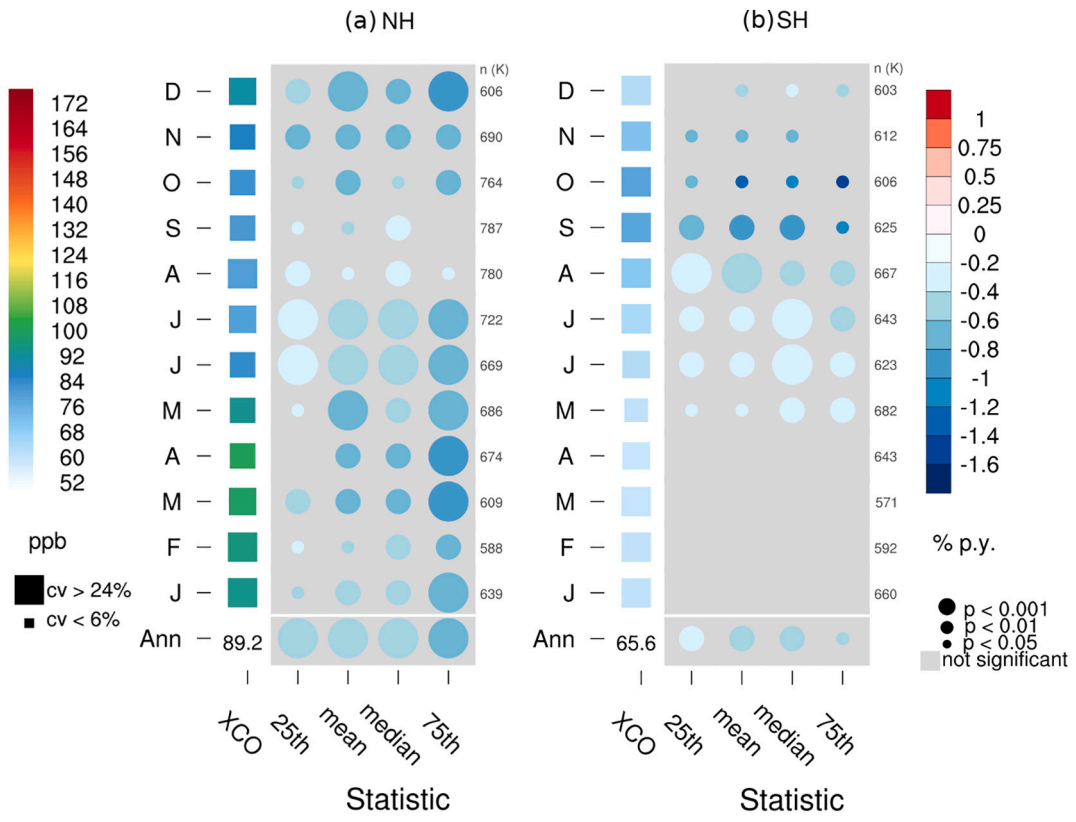

Fig. 8. Same as Fig. 7, but for (a) NH and (b) SH.

5. Conclusions

We use long-term measurements of MOPITT CO and MODIS AOD, taken from the Terra satellite, launched in December, 1999, to estimate global and regional trends in atmospheric pollution. Principal results from our study are summarized below:

1) We find a decreasing global trend in CO total column: −0.50 (±0.3) % per year over 2002 to 2018. This trend represents a global slow-down in the CO decline as compared to CO trends from earlier studies over shorter periods that found a trend of −1% per year. We attribute the slow-down to a reduced negative trend in recent years by comapring trends for 2002–2010 with 2010–2018.
2) All the TIR CO satellite records from MOPITT, AIRS, TES, IASI-A/B and CrIS observe the same hemispheric seasonality and interannual variations. This provides confidence in the MOPITT record for our subsequent detailed trend estimates. The AIRS CO NH and SH trends agree with MOPITT, while the other satellite instrument records are of insufficient length or lack processing consistency to allow for confident computation of trends.
3) Due to the shorter lifetime of aerosol, global trends in AOD were not significant. However, significant regional trends in AOD help interpret CO variability for areas with common sources, as in fire-prone regions, or where there are impacts due to air quality regulations. CO and AOD concurrently decrease in North America, Europe, and more recently, China. India has increasing trends in AOD and negligible trends in CO, indicating regional CO emissions are sufficiently large to counteract the global declining CO background.
4) Analyses of trends by percentile and month indicate that the strongest (most negative) trends occur in the 75th percentile for the NH and that late summertime CO trends (when CO lifetime is shortest) are the least significant, in both hemispheres.

Overall, local contributions from human pollution or fire emissions can counteract the global downward trend in CO. In particular, the climate-driven positive fire trend in the NH boreal fire-prone regions during summer locally counteracts the global downward CO trend and may also have hemispheric impacts through subsequent transport. Monitoring changes in regions with high local emissions will be critical for diagnosing future air quality and informing mitigation efforts.

Supplementary data to this article can be found online at https://doi.org/10.1016/j.rse.2020.112275.

Data statement

All satellite data are publicly available. Please see Table 1 and Section 2.1.2 for links to data sources. NH and SH month average CO from all the instruments are available at NCAR RDA (doi in progress). The regional month average CO for each region (along with statistics and metadata) can also be found at NCAR RDA (doi in progress).

Author contributions

Conceptualization: RRB and HMW led the design of the study; Data curation: RRB, MP and HMW collated and processed satelilte data, JW and ZW provided the AIRS data, CC, MG, PFC and DH provided the IASI data, KWB, ML, VHP, JW and SK provided the TES and CrIS data; Formal analysis: RRB performed the CO trend analysis, HMW computed CO trend maps, MP performed the AOD trend analysis, GF worked on trend error estimation and CrIS monthly means, MD, DPE, LKE, BG, JG, SMA and JRD provided guidance with MOPITT data and interpretation of results, MC and RL advised on MODIS AOD analysis and the interpretation of AOD distributions and trends; Methodology: RRB, HMW, MP, GF, MD; Visualization: RRB, HMW, MP, GF; Writing - original draft: RRB and HMW wrote and prepared the original draft, MP led discussions on aerosols, GF led appendix A1.2, WT led the discussion of trends in China, RK led the discussion of trends in India; Writing - review & editing: All authors contributed.

Declaration of Competing Interest

The authors declare that they have no known competing financial interests or personal relationships that could have appeared to influence the work reported in this paper.

Acknowledgements

The National Center for Atmospheric Research (NCAR) is sponsored by the National Science Foundation. The NCAR MOPITT project is supported by the National Aeronautics and Space Administration (NASA) Earth Observing System (EOS) Program. The MOPITT team also acknowledges support from the Canadian Space Agency (CSA), the Natural Sciences and Engineering Research Council (NSERC) and Environment Canada, and the contributions of COMDEV (the prime contractor) and ABB BOMEM. This work was funded by NASA ROSES TASNPP, contract 80NSSC18K0687. Part of this research was carried out at the Jet Propulsion Laboratory, California Institute of Technology, under a contract with NASA. TES data are available from the NASA Langley Research Center Atmospheric Science Data Center. IASI is a joint mission of EUMETSAT and the Centre National D'Etudes Spatiales (CNES, France). The IASI L1 and L2 input data are distributed in near real time by EUMETSAT through the EUMETCast system distribution. The IASI team also acknowledges the French Aeris atmospheric database (https://iasi.aeris-data.fr/) for providing the IASI L1C data and L2 data disseminated via EUMETCast, as well as CNES and CNRS for financial support. This work is also part of the EUMETSAT/AC SAF project. The research on IASI was also supported by the Belgian Science Policy Office (BELSPO) and the European Space Agency (ESA) (Prodex arrangement IASI.Flow). MODIS is a sensor aboard NASA's Terra and Aqua satellite missions. Native resolution L1B, L2 aerosol retrievals, and the gridded L3 atmospheric product used here (MOD08_M3) are all distributed via the LAADS DAAC (https://ladsweb.modaps.eosdis.nasa.gov/). We thank NCAR internal reviewers William Randel and Douglas Kinnison for their valuable suggestions.

Appendix A. Uncertainties in MOPITT CO trend analysis

Uncertainties due to the instrument system are investigated in this section. Systematic and random sampling uncertainty is assessed by determining trends in a priori and using bootstrap sampling, respectively. Systematic uncertainties due to instrument sensitivity changes are investigated using the averaging kernels.

A.1. Sampling bias

A.1.1. Approximating systematic sampling uncertainty

Sampling changes may occur for the satellite instrument over time, for example, changes due to physical scene differences such as from cloud screening. Fig. A1 shows how sampling differences on different days and months can affect the mean values in MOPITT a priori, which are taken from climatology and have no interannual variability. Differences can be seen in the $1^\circ \times 1^\circ$ gridboxes containing no data (gray) as well as differences in some gridbox colors. For instance, October 2018 sees persistent clouds over central southern China which is not the case in 2002. These differences impact how the a priori was sampled, corresponding with each MOPITT observation. While we do not necessarily expect changes in sampling over time, we use trend analysis on the sampled a priori values to approximate the impact of any systematic sampling changes within each region. This could be of particular importance for regions with large CO spatial variability, such as China.

Trends are calculated in the same way as the main text using WLS on a priori anomalies, weighted by monthly standard deviation within each region (Table A1.1). We also perform Theil-Sen analysis on year average a priori anomalies from 2002–2018 to determine trend consistency. Overall, we find no significant trends in the sampled a priori for any of the regions or time periods. Thus, we can be confident that systematic changes in sampling are not contributing to the trend analysis performed in the main text.

A.1.2. Approximating random sampling uncertainty

We estimate random sampling errors in our trend estimate by resampling MOPITT CO within regions using the bootstrap method of resampling with replacement (Efron, 1979) following the implementation of Reuter et al. (2014) and Jiang et al. (2018). This procedure randomly creates one hundred resampled datasets, to produce an ensemble of trends from which we calculate a mean trend and standard deviation.

Specifically, the method proceeds as follows: beginning with a given MOPITT level 2 dataset for a particular month and region, which contains N retrievals within the region, we construct a resampled dataset of N points by uniformly sampling the original data, with replacement. Consequently, there may be multiples of some of the original data within a resampled dataset; there may also be values in the original dataset that do not appear in the resampled dataset. This method effectively randomly increases (multiples) and decreases (left out) the weight of retrievals when contributing to the region mean. Regional means and standard deviation are calculated from the resampled dataset and time series of monthly means with corresponding standard deviations are built. We repeat this resampling process on the original data one hundred times to create an ensemble of one hundred time series, and in turn an ensemble of one hundred fitted trends for each region. Finally, we calculate a mean trend and a standard deviation over the ensemble. The standard deviation of the resampled slopes is our measure of the trend uncertainty due to resampling, which is summarized for all regions over 2002–2018 in Table A4.1:.

We have also tested the extent to which MOPITT data can be sub-sampled and still provide equivalent mean monthly values for the total column. Fig. A2 shows that selecting every 2^8 retrieval within the NH still gives the same values for the monthly mean CO column with acceptable standard error. These results informed the sub-sampling used for CrIS data processing with the MUSES algorithm.

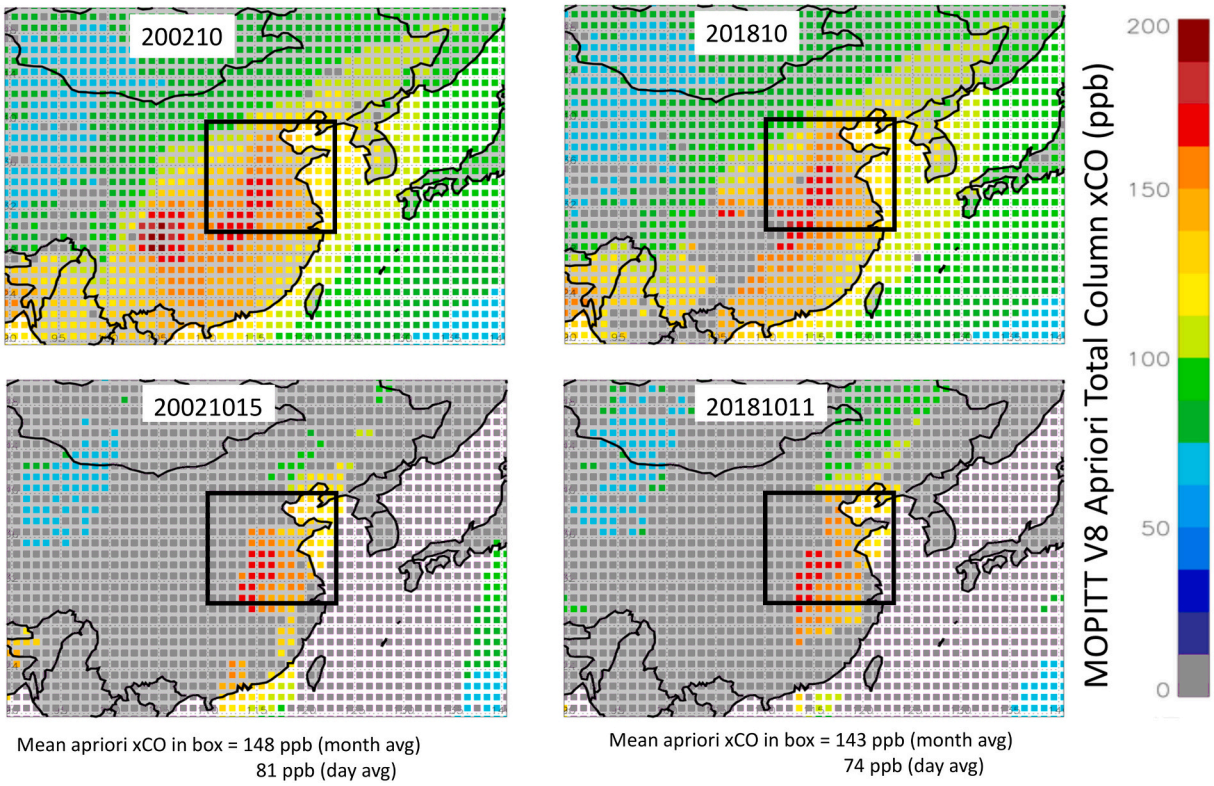

Fig. A1. MOPITT a priori total column X_{CO} for month averages (top row) and daily averages (bottom row) comparing October 2002 with October 2018. Note that daily dates were chosen to display the same MOPITT orbital swaths. The square black box is the Northeast China industrial region of interest for this study and average X_{CO} within this region is noted.

Table A1.1
Summary of WLS trends in the a priori X_{CO} anomalies for the 19 regions, shown for different time periods. Theil-Sen trends are also shown for the full time series.

	Theil-Sen (p)	WLS Trend % per year (± standard error)		
	CO			
	2002-2018	Full July 2002- June 2018	1st half July 2002- June 2010	2nd half July 2010- June 2018
Industrial				
1. NE China	-0.005 (0.84)	0.031 (0.07)	0.07 (0.2)	0.09 (0.2)
2. N India	-0.033 (0.59)	-0.02 (0.1)	0.09 (0.3)	-0.11 (0.3)
3. Europe	-0.006 (0.65)	-0.001 (0.03)	-0.06 (0.1)	0.072 (0.09)
4. E USA	-0.004 (0.71)	0.0003 (0.03)	-0.005 (0.1)	0.02 (0.1)
Fire-prone				
5. NW USA	0.004 (0.59)	0.001 (0.02)	-0.014 (0.07)	0.013 (0.06)
6. NW Canada	-0.0008 (0.90)	-0.0028 (0.006)	0.002 (0.02)	-0.020 (0.02)
7. Siberia	-0.004 (0.71)	-0.012 (0.01)	0.019 (0.03)	-0.001 (0.04)
8. Russia	-0.007 (0.34)	-0.012 (0.05)	-0.01 (0.1)	-0.02 (0.1)
9. Cent. America	0.004 (0.15)	0.005 (0.03)	0.021 (0.08)	-0.002 (0.08)
10. S America	-0.006 (0.97)	0.02 (0.2)	-0.07 (0.5)	0.05 (0.5)
11. SAm Tspt BB	0.002 (0.59)	0.001 (0.04)	-0.01 (0.1)	-0.002 (0.1)
12. Central Africa	-0.001 (0.97)	-0.016 (0.06)	-0.01 (0.2)	0.06 (0.2)
13. Southern Africa	-0.001 (0.97)	0.002 (0.09)	-0.11 (0.2)	0.03 (0.2)
14. SAf Tspt	-0.004 (0.90)	-0.01 (0.1)	0.08 (0.3)	-0.03 (0.4)
15. Maritime SEA	0.014 (0.48)	0.02 (0.1)	0.11 (0.4)	-0.01 (0.4)
16. NW Australia	-0.001 (0.90)	0.011 (0.03)	0.04 (0.1)	0.01 (0.1)
17. E Australia	0.002 (0.59)	0.006 (0.08)	0.01 (0.2)	0.02 (0.2)
Background				
18. NH (0 to 60)	-0.002 (0.59)	-0.001(0.07)	0.01 (0.2)	0.01 (0.2)
19. SH (-60 to 0)	-0.003 (0.54)	0.001 (0.2)	-0.02 (0.7)	0.01 (0.7)

Yellow backgrounds denote no significant trend for WLS analysis, relative to the slope standard error. Orange background indicates $p > 0.05$ in Theil-Sen trends.

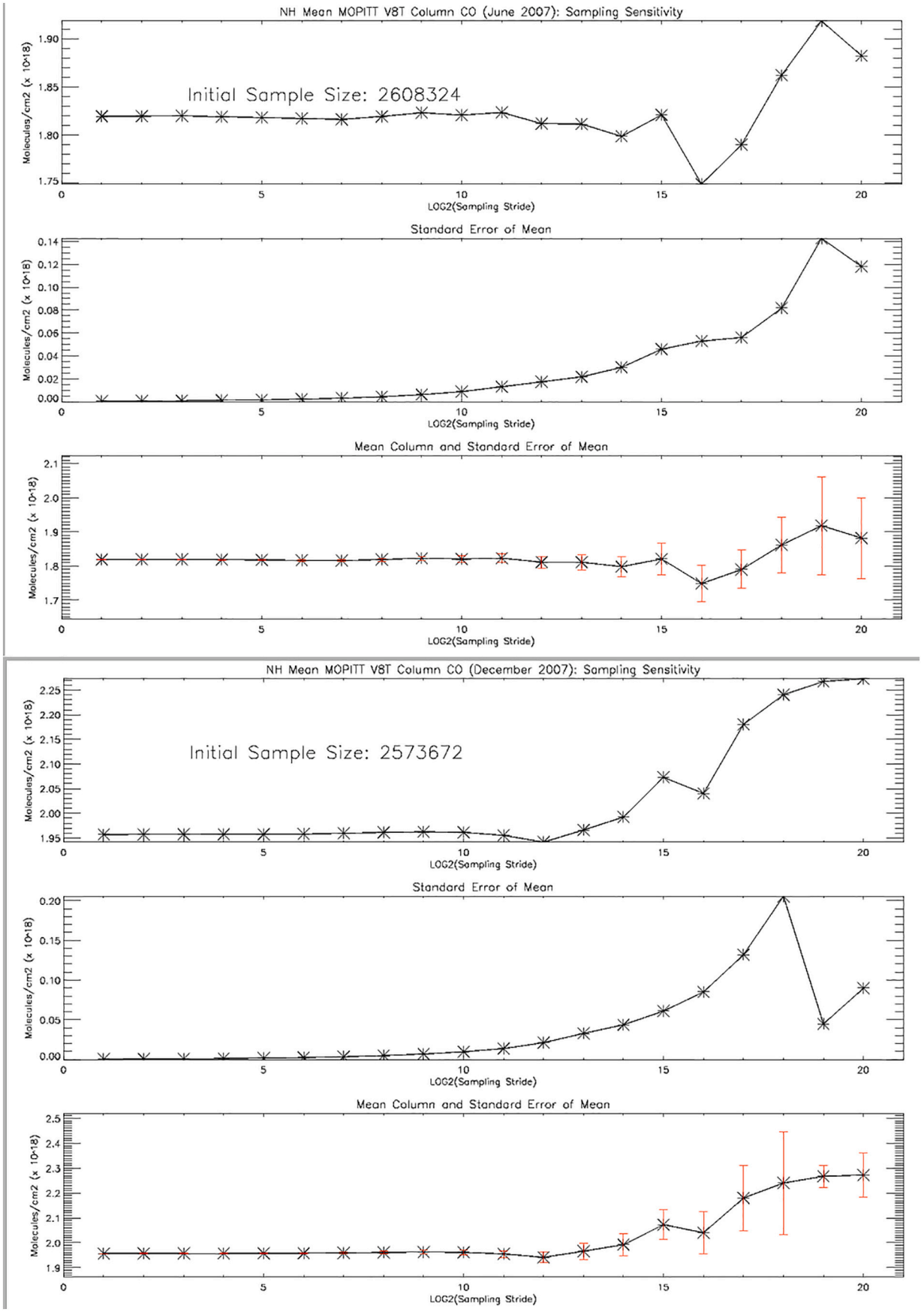

Fig. A2. Changes in MOPITT monthly mean total column CO and standard error as a function of sub-sampling reduction factor (2^n). Top three plots show results for NH June 2007 and bottom three plots show NH December 2007.

Table A2.1
Summary of estimated CO trends due to changes in MOPIT sensitivity. WLS trends in the anomalies of smoothed reanalysis climatology from the 19 regions are shown with standard error over the full, 1st half and 2nd half time periods.

	Theil-Sen (p)	WLS Trend % per year (± standard error)		
	CO			
	July 2002- June 2018	Full July 2002- June 2018	1st half July 2002- June 2010	2nd half July 2010- June 2018
Industrial				
1. NE China	0.125 (0.0001)	0.145 (0.07)	0.18 (0.2)	0.12 (0.2)
2. N India	0.016 (0.65)	0.04 (0.1)	0.20 (0.4)	0.02 (0.3)
3. Europe	-0.041 (0.02)	-0.047 (0.02)	-0.040 (0.07)	-0.031 (0.07)
4. E USA	0.024 (0.23)	-0.032 (0.02)	0.024 (0.06)	-0.014 (0.06)
Fire-prone				
5. NW USA	-0.063 (0.001)	-0.079 (0.04)	-0.14 (0.1)	-0.072 (0.1)
6. NW Canada	-0.058 (0.003)	-0.0403 (0.007)	-0.049 (0.02)	-0.032 (0.02)
7. Siberia	-0.030 (0.02)	-0.007 (0.01)	0.031 (0.03)	0.031 (0.03)
8. Russia	-0.095 (1.5e-05)	-0.065 (0.03)	-0.104 (0.07)	-0.122 (0.07)
9. Cent. America	-0.003 (0.77)	0.018 (0.03)	0.070 (0.09)	0.014 (0.09)
10. S America	0.105 (0.003)	0.05 (0.1)	0.05 (0.3)	0.09 (0.4)
11. SAm Tspt BB	-0.046 (0.02)	-0.013 (0.08)	-0.02 (0.2)	0.003 (0.2)
12. Central Africa	0.002 (0.84)	0.013 (0.03)	0.02 (0.08)	0.036 (0.09)
13. Southern Africa	-0.016 (0.30)	-0.04 (0.1)	-0.07 (0.3)	-0.02 (0.3)
14. SAf Tspt	-0.001 (1)	-0.008 (0.06)	0.06 (0.2)	-0.05 (0.2)
15. Maritime SEA	0.157 (0.02)	0.135 (0.06)	0.22 (0.2)	0.07 (0.2)
16. NW Australia	-0.005 (0.84)	0.004 (0.03)	0.02 (0.1)	-0.045 (0.09)
17. E Australia	-0.029 (0.13)	-0.001 (0.09)	0.004 (0.3)	0.011 (0.2)
Background				
18. NH (0 to 60)	-0.037 (0.006)	-0.01 (0.1)	-0.0003 (0.3)	-0.01 (0.3)
19. SH (-60 to 0)	-0.019 (0.06)	-0.01 (0.2)	-0.05 (0.6)	0.006 (0.6)

Theil-Sen trends are also shown for the full time series. Red background colors denote positive trends, blue denote negative trends and yellow background denote no trend for WLS analysis. Orange background indicates $p > 0.05$ for Theil-Sen.

A.2. Systematic uncertainty due to MOPITT sensitivity changes

Sampling may also be affected by changes in instrumental sensitivity, such as through degradation of the instrument over time. Some of this degradation of performance is known (e.g. cell gas loss) and is accounted for in the retrieval algorithm. Additionally, MOPITT retrieval sensitivity is related to the amount of atmospheric trace gas, so it would be expected to decline as CO concentrations decline, similar to changes in sensitivity for satellite temperature retrievals with increasing CO_2 (Shine et al., 2008). Sensitivity changes will be reflected in the instrument averaging kernels (AK). The degrees of freedom for signal (DFS) is a measure derived from the AK. Yoon et al. (2013), show that time varying AKs add uncertainty to trend analysis in MOPITT surface retrievals and Strode et al. (2016) found that MOPITT AKs impacted simulated trends. We examine the hemispheric DFS over time (Fig. A3) and find trend behavior that suggests we should quantify the impact of sensitivity changes on trend analysis for column values. The decreasing DFS over time corresponds with an increase in instrument noise (Deeter et al., 2015), whereby changes in instrument signals contribute to a trend in the DFS. However, although the DFS shows a strong trend over 2001–2018, we do not expect large impacts on X_{CO} trends because the DFS values remain above 1, and consequently enough information is available to retrieve column amounts.

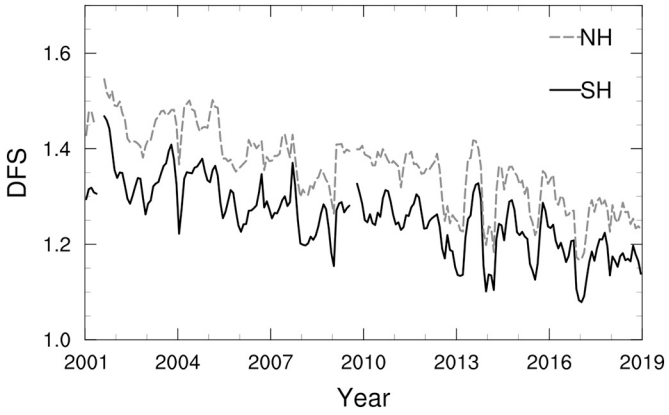

Fig. A3. Time series of degrees of freedom of signal (DFS) for MOPITT in the NH (dashed grey) and SH (solid black).

To test the impact of sensitivity changes on X_{CO} we create a global climatology from reanalysis (Gaubert et al., 2016; Gaubert et al., 2017; Gaubert and Worden, 2017), and convolve with the MOPITT monthly level-3 AKs and a priori (Eqn A1), before calculating regional averages and standard deviation and performing trend analysis. The MOPITT AKs are changing in time, while the climatology has no interannual variability. As we saw in Appendix A1.1, the a priori have no significant trends. Therefore, any trends found in the smoothed climatology are a result of sensitivity changes.

$$\mathrm{col}_{vmr_{smooth}} = \frac{(c_a + A(x_r - x_a))}{c_d} \tag{A1}$$

where:

$col_{vmr_{smooth}}$ = smoothed climatology column average VMR
c_a = MOPITT a priori column
A = MOPITT column averaging kernel
x_r = reanalysis profile in log(VMR)
x_a = MOPITT a priori profile in log(VMR)
c_d = MOPITT reported column of dry air

Trends on the smoothed reanalysis climatology for each region and time period are shown in Table A2.1, which have been calculated on anomalies with WLS in the same way as trends in the main text, weighted by regional monthly standard deviation in the smoothed data. We also perform Theil-Sen analysis on year average values from 2002–2018. Some regions show significant trends in the smoothed reanalysis, meaning that instrument sensitivity could have impacted the trend analysis performed in the main text. Significant trends with $p < 0.05$ for the Theil-Sen analysis are generally consistent with the trends that are outside one standard error in the WLS slope.

In particular, the full time series analysis over Northeast China, Europe and Eastern USA, as well as full and shorter time periods for the NH boreal fire-prone regions and Maritime SEA may have been impacted by instrument sensitivity. In most of these regions the impact is small compared to the trend in X_{CO}, however the uncertainty has been noted in Section 3.4 as a systematic error. When reported as systematic errors, they impact the trend in the opposite direction as shown in Table A2.1. For example, we see a slightly positive trend (+0.145% per year) in the smoothed reanalysis for China over 2002–2018 that indicates some of the observed negative trends could have been counteracted by instrument sensitivity. Therefore, we report a systematic error of −0.145 % per year for this effect on the regional trend.

A.3. Accounting for Autocorrelation

Autocorrelation in the noise ($\epsilon(t)$ of Equation 1) may impact the precision of the slope calculations. We determine autocorrelation in our monthly timeseries by performing autocorrelation function (ACF) analysis in the residuals, i.e. once the seasonality and trends have been removed. Residuals generally show autocorrelation indicative of an first-order autoregressive, AR(1), model process. For example, the autocorrelation function for CO in the Northern Hemisphere (NH) region is shown in Fig. A4, and is similar to an AR(1) model example with the equivalent coefficient (ϕ).

Table A3.1
Standard error estimate on the slope accounting for autocorrelation according to Eqn A2. Yellow background indicates higher errors than the WLS estimate.

	Trend % per year (± standard error + systematic error)					
	CO			AOD		
	Full July 2002-June 2018	1st half July 2002-June 2010	2nd half July 2010-June 2018	Full July 2002-June 2018	1st half July 2002-June 2010	2nd half July 2010-June 2018
Industrial						
1. NE China	0.1	0.4	0.3	0.4	NS	NS
2. N India	0.1	0.2	0.3	0.3	1.1	0.8
3. Europe	0.1	NS	0.3	NS	NS	0.9
4. E USA	0.1	0.3	0.4	0.6	1.7	1.5
Fire-prone						
5. NW USA	0.1	0.3	0.4	0.6	NS	2.7
6. NW Canada	0.1	0.4	0.3	NS	NS	NS
7. Siberia	0.2	0.6	0.5	1.0	3.6	NS
8. Russia	0.1	0.3	0.3	0.4	0.7	0.7
9. Central America	0.1	0.3	0.4	0.3	1.0	0.6
10. S America	0.4	1.0	1.0	1.3	3.7	3.2
11. SAm Transport	0.2	0.5	0.8	0.3	NS	0.8
12. Central Africa	0.1	0.2	0.3	0.4	NS	1.2
13. Southern Africa	0.1	0.3	0.5	0.3	NS	0.7
14. SAf Transport	0.1	NS	0.4	NS	NS	NS
15. Maritime SEA	0.4	1.0	1.3	1.0	2.3	3.4
16. NW Australia	0.3	0.7	0.7	0.4	NS	1.1
17. E Australia	0.2	0.4	0.6	0.4	1.1	1.0
Background						
18. NH (0 to 60)	0.2	0.3	0.5	Inconclusive due to land/ocean and mix of regions		
19. SH (-60 to 0)	0.2	0.4	0.5			

*Cardinal directions are abbreviated (e.g. Northeast = NE), SAm = South America, SAf = Southern Africa, SEA = Southeast Asia
NS = Autocorrelation is not significant for p = 0.01

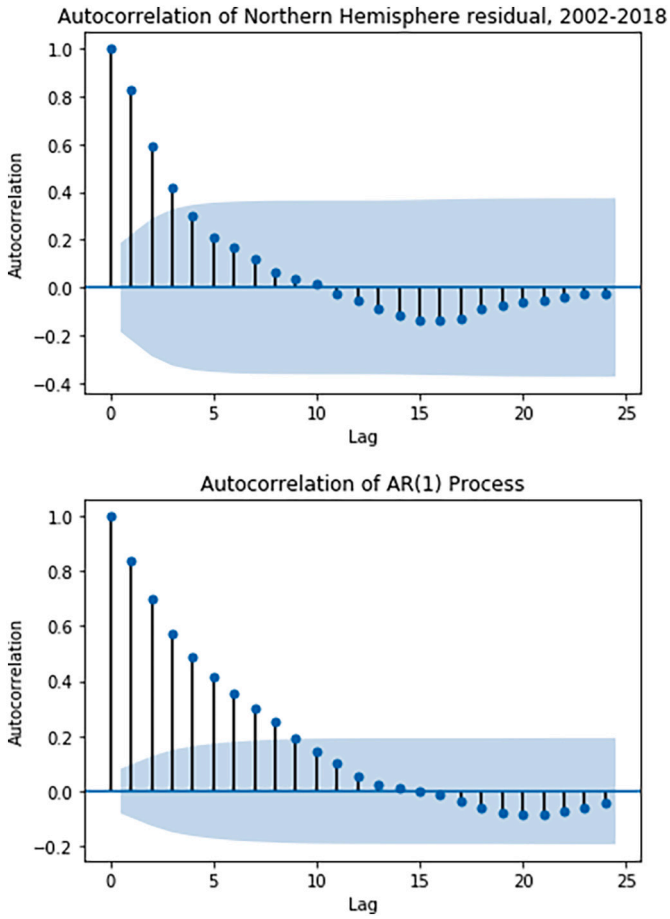

Fig. A4. Autocorrelation coefficients in monthly CO residuals for the Northern Hemisphere full timeseries (left) and autocorrelation for an AR(1) model with $\phi = 0.83$ (right). Blue shaded area shows the confidence intervals for p = 0.01.

Consequently, we compensate for an AR(1) noise process by adjusting the standard error to account for autocorrelation. According to Weatherhead et al. (1998) the standard error in the slope (σ_m) can be accurately approximated by the standard deviation in the noise (σ_ϵ), combined with a scaling factor based on the autocorrelation coefficient at lag-1, ϕ:

$$\sigma_m \approx \frac{\sigma_\epsilon}{N^{3/2}} \sqrt{\frac{1+\phi}{1-\phi}} \tag{A2}$$

where N is the number of years of data (Weatherhead et al., 1998, equation 2).

We investigate autocorrelation in the residual for all regions and where it is found to be significant outside the 99 % confidence intervals, we calculate the standard errors according to equation A2 and collect the results in Table A3.1. The estimated standard error on the slope from equation A2 was compared with the WLS standard error and was found to be of approximate similar magnitude, and generally smaller than the WLS estimate, but sometimes larger. Therefore, as a conservative estimate of the standard error on the slope, we retain the larger of the two estimates in the main section of the manuscript.

The Theil-Sen trend estimates in Section 4.2 do not require compensation for autocorrelation in the noise, because consecutive values are separated by a year and CO has about a 2 month atmopsheric lifetime, meaning persistence is not significant. For example, the residuals for January trend analysis in the NH region show no significant autocorrelation (Fig. A5), even though the NH full timeseries showed the largest autocorrelation coefficient ($\phi = 0.83$) of all datasets. Similarly, no significant autocorrelation in the residuals was found in other regions when trend analysis is completed in months across different years.

Table A4.1
Summary of uncertainties in the 2002–2018 trend analysis compared with WLS standard error in the slope. All values are shown in percent per year. Green backgrounds are significant.

	Sampling uncertainty		MOPITT sensitivity (systematic)	Std err from WLS	Approximated Std err with autocorrelation
	systematic	random			
Industrial					
1. NE China	-0.031	±0.005	-0.145	±0.3	±0.1
2. N India	+0.02	±0.003	-0.04	±0.2	±0.1
3. Europe	+0.001	±0.003	+0.047	±0.1	±0.1
4. E USA	-0.0003	±0.004	+0.032	±0.1	±0.1
Fire-prone					
5. NW USA	-0.001	±0.004	+0.079	±0.2	±0.1
6. NW Canada	+0.0028	±0.004	+0.0403	±0.1	±0.1
7. Siberia	+0.012	±0.006	+0.007	±0.1	±0.2
8. Russia	+0.012	±0.001	+0.065	±0.1	±0.1
9. Cent. America	-0.005	±0.001	-0.018	±0.1	±0.1
10. S America	-0.02	±0.002	-0.05	±0.2	±0.3
11. SAm Tspt BB	-0.001	±0.002	+0.013	±0.2	±0.2
12. Central Africa	+0.016	±0.001	-0.013	±0.2	±0.1
13. Southern Africa	-0.002	±0.002	+0.04	±0.3	±0.1
14. SAf Tspt	+0.01	±0.002	+0.008	±0.2	±0.1
15. Maritime SEA	-0.02	±0.003	-0.135	±0.2	±0.4
16. NW Australia	-0.011	±0.001	-0.004	±0.1	±0.3
17. E Australia	-0.006	±0.001	+0.001	±0.2	±0.2
Background					
18. NH (0 to 60)	+0.001	±0.0004	+0.01	±0.3	±0.2
19. SH (-60 to 0)	-0.001	±0.0005	+0.01	±0.3	±0.2

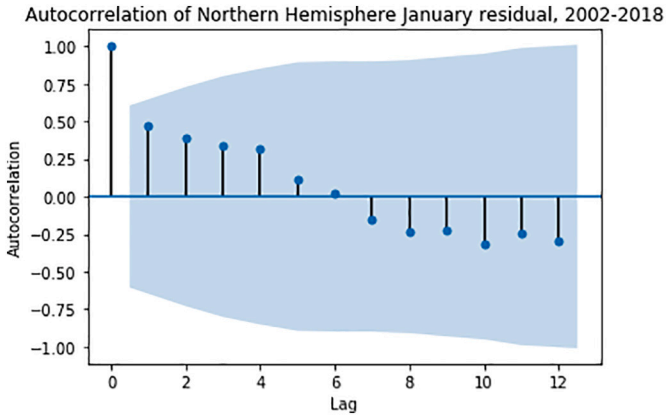

Fig. A5. Autocorrelation coefficients in monthly January residual values for the Northern Hemisphere. Blue shaded area shows the confidence intervals for p = 0.01.

A.4. Summary of uncertainties 2002–2008

A comparison between uncertainties and the WLS standard error for 2002–2018 trends is shown in Table A4.1. Systematic uncertainties are described in one direction and random uncertainty is bi-directional. The uncertainties reported here are of opposite sign to the slopes calculated in Appendix A1.1 and A2. Although in some cases uncertainties are determined significant, all uncertainties are small compared to the standard error in the slope from the main text. Overall, the impact of these uncertainties on the trends found in the main text does not alter our main findings and conclusions.

Appendix B. Other impacts on trend analysis

We investigate the robustness of trend analysis to accounting for the seasonal cycle in different ways, using different trend methodologies, as well as the impact of outliers.

B.1. Selection of trend analysis methodology

Noise is anything that deviates the data from the model (the linear trend), and consequently increases uncertainty in trend analysis. The seasonal cycle in CO data therefore adds noise to the trend analysis. There are several methods one can use to remove the impact of seasonality on trend analysis. We investigate four methods of accounting for seasonality prior to calculating the WLS trend.

Method 1: use year average values in trend calculations.

Method 2: calculate the 12-month moving average. Because seasonality occurs during a 12-month period, any shorter or longer time period (not divisible by 12) would introduce some seasonal information.

Method 3: subtract the whole dataset month average values.

Method 4: remove the seasonal cycle using a harmonic fit.

We also assess the use of Theil-Sen on year-average values. The Theil-Sen method is robust to outliers, but is sensitive to cyclic data, therefore we use yearly averages of the monthly anomaly data.

All methods calculate consistent trend signs and magnitudes within one standard error, apart from the WLS on running averages for South America (Table B1.1). Regions that show difficulty for interpreting significant trends (Southern Africa) are also generally consistent. In the main text, we choose to use Method 2 before applying WLS in global map analysis and Method 3 before applying WLS in timeseries analysis.

B.2. Impact of outliers on trend analysis

WLS trend analysis is less impacted by outliers than ordinary least squares because variability associated with outliers reduces the weight of the outlier contribution to trend analysis. However, we wish to quantify the impact of the large El Niño in 2015 on trend analysis. Fig. 3c and d show the hemispheric impact of the 2015 fires in Maritime SEA. The large contribution to atmospheric CO loading from this event remained in the atmosphere for over 2 months (Field et al., 2016). Resulting high values could have skewed our results towards less negative trends. Consequently, we investigate the impact of removing X_{CO} data from July 2015 to June 2016, and recalculate trends. The comparison between trends calculated with and without Maritime SEA fire influence in 2015 is shown in Table B2.1.

When removing the Maritime SEA event from analysis, trends become consistently more negative. Trends in the shorter period experience more impact than the longer period. Largest differences are seen around the SH fire-prone regions. However, most of the trends are not significantly different from what was calculated in the main text, relative to one standard error. Furthermore, the changes in trends do not alter our conclusions from the main text. We still find the slowdown in the CO trend such that the earlier record has a stronger trend than either the later or long-term records.

We were also interested in the large dip in 2008–2009 that might particularly influence the trends in our early sub-time period (Fig. 3c), so we removed February 2008 to January 2010 and recalculated trends (not shown). While we found some substantial differences in trend magnitudes for some regions, the overall message remained that the earlier period experienced more negative trends in CO compared to the later period or the whole time period.

Table B1.1
Summary of weighted least-squares different methods of accounting for seasonality. Theil-Sen trends are also shown for the full time series.

	Theil-Sen (p) on year average	Method 1: WLS Trend on year average (± standard error)	Method 2: WLS Trend on Runave	Method 3: WLS Trend on Anomaly (using mean annual cycle)	Method 4: WLS Trend on Anomaly (using harmonics)
	2002-2018		Full July 2002- June 2018: % per year (± standard error)		
Industrial					
1. NE China	-1.20 (2.2e-05)	-1.16 (0.3)	-1.22 (0.3)	-1.18 (0.3)	-1.18 (0.3)
2. N India	-0.19 (0.036)	-0.27 (0.1)	-0.26 (0.2)	-0.28 (0.2)	-0.28 (0.2)
3. Europe	-0.77 (3.2e-05)	-0.79 (0.2)	-0.78 (0.1)	-0.89 (0.1)	-0.88 (0.1)
4. E USA	-0.78 (1.5e-05)	-0.79 (0.2)	-0.84 (0.1)	-0.85 (0.1)	-0.84 (0.1)
Fire-prone					
5. NW USA	-0.71 (3.4e-04)	-0.80 (0.2)	-0.74 (0.2)	-0.85 (0.2)	-0.83 (0.2)
6. NW Canada	-0.59 (4.6e-04)	-0.58 (0.2)	-0.63 (0.1)	-0.60 (0.1)	-0.59 (0.1)
7. Siberia	-0.67 (1.5e-03)	-0.57 (0.2)	-0.61 (0.1)	-0.59 (0.1)	-0.58 (0.1)
8. Russia	-0.72 (1.0e-05)	-0.77 (0.2)	-0.77 (0.1)	-0.80 (0.1)	-0.79 (0.1)
9. Cent. America	-0.49 (2.0e-03)	-0.52 (0.2)	-0.48 (0.1)	-0.46 (0.1)	-0.46 (0.1)
10. S America	-0.70 (0.053)	-0.53 (0.4)	-0.70 (0.2) *	-0.31 (0.2)	-0.30 (0.2)
11. SAm Tspt BB	-0.64 (5.8e-03)	-0.53 (0.2)	-0.55 (0.2)	-0.39 (0.2)	-0.38 (0.2)
12. Central Africa	-0.23 (0.015)	-0.25 (0.1)	-0.23 (0.2)	-0.22 (0.2)	-0.22 (0.2)
13. Southern Africa	-0.26 (0.11)	-0.21 (0.2)	-0.20 (0.3)	-0.17 (0.3)	-0.17 (0.3)
14. SAf Tspt	-0.04 (0.90)	-0.08 (0.2)	0.04 (0.2)	-0.07 (0.2)	-0.07 (0.2)
15. Maritime SEA	-0.69 (0.029)	-0.71 (0.3)	-0.54 (0.2)	-0.51 (0.2)	-0.50 (0.2)
16. NW Australia	-0.49 (0.053)	-0.32 (0.3)	-0.37 (0.1)	-0.25 (0.1)	-0.25 (0.1)
17. E Australia	-0.44 (0.015)	-0.45 (0.2)	-0.42 (0.2)	-0.32 (0.2)	-0.32 (0.2)
Background					
18. NH (0 to 60)	-0.57 (4.6e-04)	-0.59 (0.1)	-0.54 (0.3)	-0.57 (0.3)	-0.56 (0.3)
19. SH (-60 to 0)	-0.47 (7.4e-03)	-0.47 (0.1)	-0.39 (0.3)	-0.35 (0.3)	-0.35 (0.3)

Blue backgrounds denote negative trends and yellow background denote no trend for WLS analysis. Orange background indicates $p > 0.05$ for Theil-Sen (non-significant). *Significantly different trend result outside one σm.

Table B2.1
Summary of WLS trends in the anomaly X_{CO} from the 19 regions with standard error in brackets, shown for different time periods. The result of removing Maritime SEA large fire emissions impact (without 201507-201606) is investigated.

	WLS Trend on Runave % per year (+/- standard error)			
	Original	Without 201507-201606	Original	Without 201507-201606
	Full July 2002-June 2018		2nd half July 2010-June 2018	
Industrial				
1. NE China	-1.18 (0.3)	-1.26 (0.3)	-1.02 (0.7)	-1.14 (0.7)
2. N India	-0.28 (0.2)	-0.34 (0.2)	-0.17 (0.5)	-0.29 (0.5)
3. Europe	-0.89 (0.1)	-1.00 (0.1)	-0.47 (0.3)	-0.67 (0.3)
4. E USA	-0.85 (0.1)	-0.98 (0.1)	-0.73 (0.3)	-0.95 (0.3)
Fire-prone				
5. NW USA	-0.85 (0.2)	-0.95 (0.2)	-0.67 (0.4)	-0.85 (0.4)
6. NW Canada	-0.60 (0.1)	-0.67 (0.1)	-0.51 (0.3)	-0.64 (0.3)
7. Siberia	-0.59 (0.1)	-0.64 (0.1)	-0.32 (0.4)	-0.40 (0.4)
8. Russia	-0.80 (0.1)	-0.88 (0.1)	-0.66 (0.3)	-0.81 (0.3)
9. Cent. America	-0.46 (0.1)	-0.58 (0.1)	-0.23 (0.4)	-0.46 (0.4)
10. S America	-0.31 (0.2)	-0.40 (0.2)	0.02 (0.6)	-0.16 (0.6)
11. SAm Tspt BB	-0.39 (0.2)	-0.48 (0.2)	-0.03 (0.5)	-0.24 (0.5)
12. Central Africa	-0.22 (0.2)	-0.27 (0.2)	-0.12 (0.5)	-0.21 (0.5)
13. Southern Africa	-0.17 (0.3)	-0.29 (0.3)	-0.09 (0.7)	-0.34 (0.7)
14. SAf Tspt	-0.07 (0.2)	-0.18 (0.2)	0.14 (0.6)	-0.08 (0.6)
15. Maritime SEA	-0.51 (0.2)	-0.63 (0.2)	-0.14 (0.5)	-0.34 (0.5)
16. NW Australia	-0.25 (0.1)	-0.34 (0.1)	0.03 (0.4)	-0.15 (0.4)
17. E Australia	-0.32 (0.2)	-0.42 (0.2)	0.16 (0.5)	-0.01 (0.5)
Background				
18. NH (0 to 60)	-0.57 (0.3)	-0.67 (0.3)	-0.43 (0.8)	-0.63 (0.8)
19. SH (-60 to 0)	-0.35 (0.3)	-0.46 (0.4)	-0.1 (1)	-0.3 (1)

The original record values are the same as found in Table 2. Trends without 201507–201606 removes the extended influence from the large fires in Maritime SEA during the burning season of 2015. Green background colors indicate differences outside one standard error.

References

AIRS Science Team/Joao Teixeira, 2013. AIRS/Aqua L2 Standard Physical Retrieval (AIRS-only) V006. Goddard Earth Sciences Data and Information Services Center (GES DISC), Greenbelt, MD, USA. https://doi.org/10.5067/Aqua/AIRS/DATA202. Accessed: [31 October, 2019].

Andela, N., Morton, D.C., Giglio, L., Chen, Y., van der Werf, G.R., Kasibhatla, P.S., DeFries, R.S., Collatz, G.J., Hantson, S., Kloster, S., Bachelet, D., Forrest, M., Lasslop, G., Li, F., Mangeon, S., Melton, J.R., Yue, C., Randerson, J.T., 2017. A human-driven decline in global burned area. Science 356 (6345), 1356–1362. https://doi.org/10.1126/science.aal4108.

Arellano, A.F., Hess, P.G., Edwards, D.P., Baumgardner, D., 2010. Constraints on black carbon aerosol distribution from Measurement of Pollution in the Troposphere (MOPITT) CO. Geophys. Res. Lett. 37 (17), 17801. https://doi.org/10.1126/science.aal4108.

Aumann, H.H., Chahine, M.T., Gautier, C., Goldberg, M.D., Kalnay, E., McMillin, L.M., Revercomb, H., Rosenkranz, P.W., Smith, W.L., Staelin, D.H., Strow, L.L., Susskind, J., 2003. AIRS/AMSU/HSB on the Aqua mission: design, science objectives, data products, and processing systems. IEEE Trans. Geosci. Remote Sens. 41 (2), 253–264. https://doi.org/10.1109/TGRS.2002.808356.

Beer, R., 2006. TES on the aura mission: scientific objectives, measurements, and analysis overview. IEEE Trans. Geosci. Remote Sens. 44, 1102–1105. https://doi.org/10.1109/TGRS.2005.863716.

Bhardwaj, P., Naja, M., Kumar, R., Chandola, H.C., 2016. Seasonal, interannual and long term variabilities in biomass burning activity over South Asia. Environ. Sci. Pollut. R. 23, 4397–4410. https://doi.org/10.1007/s11356-015-5629-6.

Bowman, K., Henze, D.K., 2012. Attribution of direct ozone radiative forcing to spatially resolved emissions. Geophys. Res. Lett. 39 (22), L22704 https://doi.org/10.1029/2012GL053274.

Bowman, K.W., Rodgers, C.D., Kulawik, S.S., Worden, J., Sarkissian, E., Osterman, G., Steck, T., Lou, M., Eldering, A., Shephard, M., Worden, H., Lampel, M., Clough, S., Brown, P., Rinsland, C., Gunson, M., Beer, R., 2006. Tropospheric emission spectrometer: retrieval method and error analysis. IEEE Trans. Geosci. Remote Sens. 44, 1297–1307. https://doi.org/10.1109/TGRS.2006.871234.

Buchholz, R.R., Deeter, M.N., Worden, H.M., Gille, J., Edwards, D.P., Hannigan, J.W., Jones, N.B., Paton-Walsh, C., Griffith, D.W.T., Smale, D., Robinson, J., Strong, K., Conway, S., Sussmann, R., Hase, F., Blumenstock, T., Mahieu, E., Langerock, B., 2017. Validation of MOPITT carbon monoxide using ground-based fourier transform infrared spectrometer data from NDACC. Atmos. Meas. Tech. 10 (5), 1927–1956. https://doi.org/10.5194/amt-10-1927-2017.

Buchholz, R.R., Hammerling, D., Worden, H.M., Deeter, M.N., Emmons, L.K., Edwards, D.P., Monks, S.A., 2018. Links between carbon monoxide and climate indices for the southern hemisphere and tropical fire regions. J. Geophys. Res.-Atmos. 123 (17), 9786–9800. https://doi.org/10.1029/2018JD028438.

Clerbaux, C., Boynard, A., Clarisse, L., George, M., Hadji-Lazaro, J., Herbin, H., Hurtmans, D., Pommier, M., Razavi, A., Turquety, S., Wespes, C., Coheur, P.-F., 2009. Monitoring of atmospheric composition using the thermal infrared IASI/MetOp sounder. Atmos. Chem. Phys. 9, 6041–6054. https://doi.org/10.5194/acp-9-6041-2009.

de Ruyter de Wildt, M., Eskes, H., Boersma, K.F., 2012. The global economic cycle and satellite-derived NO2 trends over shipping lanes. Geophys. Res. Lett. 39, L01802 https://doi.org/10.1029/2011GL049541.

Deeter, M.N., Emmons, L.K., Francis, G.L., Edwards, D.P., Gille, J.C., Warner, J.X., Khattatov, B., Ziskin, D., Lamarque, J.-F., Ho, S.P., Yudin, V., Attie, J.L., Packman, D., Chen, J., Mao, D., Drummond, J.R., Novelli, P., Sachse, G., 2004. Evaluation of operational radiances for the Measurements of Pollution in the Troposphere (MOPITT) instrument CO thermal band channels. J.Geophys. Res. 109, D03308 https://doi.org/10.1029/2003JD003970.

Deeter, M.N., Martínez-Alonso, S., Edwards, D.P., Emmons, L.K., Gille, J.C., Worden, H.M., Pittman, J.V., Daube, B.C., Wofsy, S.C., 2013. Validation of MOPITT Version 5 thermal-infrared, near-infrared, and multispectral carbon monoxide profile retrievals for 2000–2011. J. Geophys. Res. Atmos. 118, 6710–6725. https://doi.org/10.1002/jgrd.50272.

Deeter, M.N., Edwards, D.P., Gille, J.C., Worden, H.M., 2015. Information content of MOPITT CO profile retrievals: Temporal and geographical variability. J. Geophys. Res. Atmos. 120 (12), 723–738. https://doi.org/10.1002/2015JD024024.

Deeter, M.N., Martínez-Alonso, S., Andreae, M.O., Schlager, H., 2018. Satellite-based analysis of CO seasonal and interannual variability over the Amazon Basin. J. Geophys. Res.-Atmos. 123, 5641–5656. https://doi.org/10.1029/2018JD028425.

Deeter, M.N., Edwards, D.P., Francis, G.L., Gille, J.C., Mao, D., Martinez-Alonso, S., Worden, H.M., Ziskin, D., Andreae, M.O., 2019. Radiance-based retrieval bias mitigation for the MOPITT instrument: the version 8 product. Atmos. Meas. Tech. 12 (8), 4561–4580. https://doi.org/10.5194/amt-12-4561-2019.

Dennison, P.E., Brewer, S.C., Arnold, J.D., Moritz, M.A., 2014. Large wildfire trends in the western United States, 1984–2011. Geophys. Res. Lett. 41, 2928–2933. https://doi.org/10.1002/2014GL059576.

Drummond, J.R., Zou, J., Nichitiu, F., Kar, J., Deschambaut, R., Hackett, J., 2010. A review of 9-year performance and operation of the MOPITT instrument. Adv. Space Res. 45 (6), 760–774. https://doi.org/10.1016/j.asr.2009.11.019.

Edwards, D.P., Emmons, L.K., Hauglustaine, D.A., Chu, D.A., Gille, J.C., Kaufman, Y.J., Pétron, G., Yurgano, L.N., Giglio, V.L., Deeter, M.N., Yudi, V., Ziskin, N.D.C., Warner, J., Lamarque, J.-F., Francis, G.L., Ho, S.P., Mao, D., Chen, J., Grechk, E.I., Drummond, O.J.R., 2004. Observations of carbon monoxide and aerosols from the terra satellite: northern hemisphere variability. J. Geophys. Res.-Atmos. 109 (D24) https://doi.org/10.1029/2004JD004727.

Edwards, D.P., Emmons, L.K., Gille, J.C., Chu, A., Attié, J.-L., Giglio, L., Wood, S.W., Haywood, J., Deeter, M.N., Massie, S.T., Ziskin, D.C., Drummond, J.R., 2006. Satellite-observed pollution from Southern Hemisphere biomass burning. J. Geophys. Res. 111, D14312 https://doi.org/10.1029/2005JD006655.

Efron, B., 1979. Bootstrap Methods: Another Look at the Jackknife. Ann. Stat. 7 (1), 1–26. https://doi.org/10.1214/aos/1176344552.

Field, R.D., van der Werf, G.R., Fanin, T., Fetzer, E.J., Fuller, R., Jethva, H., Levy, R., Livesey, N.J., Luo, M., Torres, O., Worden, H.M., 2016. Indonesian fire activity and smoke pollution in 2015 show persistent nonlinear sensitivity to El Nino-induced drought. Proc. Natl. Acad. Sci. U. S. A. 113 (33), 9204–9209. https://doi.org/10.1073/pnas.1524888113.

Filonchyk, M., Yan, H., Zhang, Z., Yang, S., Li, W., Li, Y., 2019. Combined use of satellite and surface observations to study aerosol optical depth in different regions of China. Sci. Rep. 9, 6174. https://doi.org/10.1038/s41598-019-42466-6.

Fu, D., Bowman, K.W., Worden, H.M., Natraj, V., Worden, J.R., Yu, S., Veefkind, P., Aben, I., Landgraf, J., Strow, L., Han, Y., 2016. High-resolution tropospheric carbon monoxide profiles retrieved from CrIS and TROPOMI. Atmos. Meas. Tech. 9 (6), 2567–2579. https://doi.org/10.5194/amt-9-2567-2016.

Gambacorta, A., 2013. The NUCAPS algorithm theoretical basis documentation 2013 [Online]. https://www.ospo.noaa.gov/Products/atmosphere/soundings/nucaps/docs/NUCAPS_ATBD_20130821.pdf.

Gambacorta, A., Barnet, C., Wolf, W., King, T., Maddy, E., Strow, L., Xiong, X., Nalli, N., Goldberg, M., 2014. An experiment using high spectral resolution CrIS measurements for atmospheric trace gases: carbon monoxide retrievals impact study. IEEE Geosci. Remote S. 11, 1639–1643. https://doi.org/10.1109/LGRS.2014.2303641.

Gaubert, B., Worden, H., 2017. NCAR/MOPITT Reanalysis, Research Data Archive at the National Center for Atmospheric Research, Computational and Information Systems Laboratory. https://doi.org/10.5065/D6SB44GZ (Accessed 13 Sep 2019).

Gaubert, B., Arellano, A.F., Barré, J., Worden, H.M., Emmons, L.K., Tilmes, S., Buchholz, R.R., Vitt, F., Raeder, K., Collins, N., Anderson, J.L., Wiedinmyer, C., Martinez Alonso, S., Edwards, D.P., Andreae, M.O., Hannigan, J.W., Petri, C., Strong, K., Jones, N., 2016. Toward a chemical reanalysis in a coupled chemistry-climate model: An evaluation of MOPITT CO assimilation and its impact on tropospheric composition. J. Geophys. Res. Atmos. 121, 7310–7343. https://doi.org/10.1002/2016JD024863.

Gaubert, B., Worden, H.M., Arellano, A.F.J., Emmons, L.K., Tilmes, S., Barré, J., Martinez Alonso, S., Vitt, F., Anderson, J.L., Alkemade, F., Houweling, S., Edwards, D.P., 2017. Chemical feedback from decreasing carbon monoxide emissions. Geophys. Res. Lett. 44, 9985–9995. https://doi.org/10.1002/2017GL074987.

George, M., Clerbaux, C., Hurtmans, D., Turquety, S., Coheur, P.-F., Pommier, M., Hadji-Lazaro, J., Edwards, D.P., Worden, H., Luo, M., Rinsland, C., McMillan, W., 2009. Carbon monoxide distributions from the IASI/METOP mission: evaluation with other space-borne remote sensors. Atmos. Chem. Phys. 9, 8317–8330. https://doi.org/10.5194/acp-9-8317-2009.

George, M., Clerbaux, C., Bouarar, I., Coheur, P.-F., Deeter, M.N., Edwards, D.P., Francis, G., Gille, J.C., Hadji-Lazaro, J., Hurtmans, D., Inness, A., Mao, D., Worden, H.M., 2015. An examination of the long-term CO records from MOPITT and IASI: comparison of retrieval methodology. Atmos. Meas. Tech. 8 (10), 4313–4328. https://doi.org/10.5194/amt-8-4313-2015.

Ghude, S.D., Bhat, G.S., Prabhakaran, T., Jenamani, R.K., Chate, D.M., Safai, P.D., Karipot, A.K., Konwar, M., Pithani, P., Sinha, V., Rao, P.S.P., Dixit, S.A., Tiwari, S., Todekar, K., Varpe, S., Srivastava, A.K., Bisht, D.S., Murugavel, P., Ali, K., Mina, U., Dharua, M., Jaya Rao, Y., Padmakumari, B., Hazra, A., Nigam, N., Shende, U., Lal, D. M., Chandra, B.P., Mishra, A.K., Kumar, A., Hakkim, H., Pawar, H., Acharja, P., Kulkarni, R., Subharthi, C., Balaji, B., Varghese, M., Bera, S., Rajeevan, M., 2017. Winter Fog Experiment Over the Indo-Gangetic Plains of India. Curr. Sci. 112, 767–784. https://doi.org/10.18520/cs/v112/i04/767-784.

Gupta, P., Remer, L.A., Patadia, F., Levy, R.C., Christopher, S.A., 2020. High-resolution gridded level 3 aerosol optical depth data from MODIS. Remote Sens. 12, 2847. https://doi.org/10.3390/rs12172847.

Hedelius, J.K., He, T.-L., Jones, D.B.A., Baier, B.C., Buchholz, R.R., De Mazière, M., Deutscher, N.M., Dubey, M.K., Feist, D.G., Griffith, D.W.T., Hase, F., Iraci, L.T., Jeseck, P., Kiel, M., Kivi, R., Liu, C., Morino, I., Notholt, J., Oh, Y.-S., Ohyama, H., Pollard, D.F., Rettinger, M., Roche, S., Roehl, C.M., Schneider, M., Shiomi, K., Strong, K., Sussmann, R., Sweeney, C., Uchino, Y.T.O., Velazco, V.A., Wang, W., Warneke, T., Wennberg, P.O., Worden, H.M., Wunch, D., 2019. Evaluation of MOPITT Version 7 joint TIR-NIR XCO retrievals with TCCON. Atmos. Meas. Tech. 12 (10), 5547–5572. https://doi.org/10.5194/amt-12-5547-2019.

Holloway, T., Levy II, H., Kasibhatla, P., 2000. Global distribution of carbon monoxide. J. Geophys. Res. 105 (D10), 12,123–12,147. https://doi.org/10.1029/1999JD901173.

Hsu, N.C., Jeong, M.-J., Bettenhausen, C., Sayer, A.M., Hansell, R., Seftor, C.S., Huang, J., Tsay, C.-C., 2013. Enhanced deep blue aerosol retrieval algorithm: the second generation. J. Geophys. Res. Atmos. 118, 9296–9315. https://doi.org/10.1002/jgrd.50712.

Huijnen, V., Wooster, M.J., Kaiser, J.W., Gaveau, D.L.A., Flemming, J., Parrington, M., Inness, A., Murdiyarso, D., Main, B., van Weele, M., 2016. Fire carbon emissions over maritime southeast Asia in 2015 largest since 1997. Sci. Rep. 6, 26886. https://doi.org/10.1038/srep26886.

Hurtmans, D., Coheur, P.-F., Wespes, C., Clarisse, L., Scharf, O., Clerbaux, C., Hadji-Lazaro, J., George, M., Turquety, S., 2012. FORLI radiative transfer and retrieval code for IASI. J. Quant. Spectrosc. Ra. 113, 1391–1408. https://doi.org/10.1016/j.jqsrt.2012.02.036.

Jethva, H., Torres, O., Field, R.D., Lyapustin, A., Gautam, R., Kayetha, V., 2019. Connecting Crop Productivity, Residue Fires, and Air Quality over Northern India. Sci Rep 9, 16594. https://doi.org/10.1038/s41598-019-52799-x.

Jiang, Z., Worden, J.R., Worden, H., Deeter, M., Jones, D.B.A., Arellano, A.F., Henze, D. K., 2017. A 15-Year Record of CO Emissions Constrained by MOPITT CO Observations. Atmos. Chem. Phys. 17 (7), 4565–4583. https://doi.org/10.5194/acp-17-4565-2017.

Jiang, Z., McDonald, B.C., Worden, H., Worden, J.R., Miyazaki, K., Qu, Z., Henze, D.K., Jones, D.B.A., Arellano, A.F., Fischer, E.V., Zhu, L., Boersma, K.F., 2018. Unexpected slowdown of US pollutant emission reduction in the past decade. PNAS 115 (20), 5099–5104. https://doi.org/10.1073/pnas.1801191115.

Kanakidou, M., Seinfeld, J.H., Pandis, S.N., Barnes, I., Dentener, F.J., Facchini, M.C., Van Dingenen, R., Ervens, B., Nenes, A., Nielsen, C.J., Swietlicki, E., Putaud, J.P., Balkanski, Y., Fuzzi, S., Horth, J., Moortgat, G.K., Winterhalter, R., Myhre, C.E.L., Tsigaridis, K., Vignati, E., Stephanou, E.G., Wilson, J., 2005. Organic aerosol and global climate modelling: a review. Atmos. Chem. Phys. 5, 1053–1123. https://doi.org/10.5194/acp-5-1053-2005.

Kendall, M.G., 1975. Rank Correlation Methods, 4th edition. Charles Griffin, London.

Kerzenmacher, T., Dils, B., Kumps, N., Blumenstock, T., Clerbaux, C., Coheur, P.-F., Demoulin, P., García, O., George, M., Griffith, D.W.T., Hase, F., Hadji-Lazaro, J., Hurtmans, D., Jones, N., Mahieu, E., Notholt, J., Paton-Walsh, C., Raffalski, U., Ridder, T., Schneider, M., Servais, C., De Mazière, M., 2012. Validation of IASI FORLI carbon monoxide retrievals using FTIR data from NDACC. Atmos. Meas. Tech. 5, 2751–2761. https://doi.org/10.5194/amt-5-2751-2012.

King, M.D., Platnick, S., Menzel, W.P., Ackerman, S.A., Hubanks, P.A., 2013. Spatial and temporal distribution of clouds observed by MODIS onboard the Terra and Aqua satellites. IEEE Trans. Geosci. Remote Sens. 51, 3826–3852. https://doi.org/10.1109/TGRS.2012.2227333.

Klonecki, A., Pommier, M., Clerbaux, C., Ancellet, G., Cammas, J.-P., Coheur, P.-F., Cozic, A., Diskin, G.S., Hadji-Lazaro, J., Hauglustaine, D.A., Hurtmans, D., Khattatov, B., Lamarque, J.-F., Law, K.S., Nedelec, P., Paris, J.-D., Podolske, J.R., Prunet, P., Schlager, H., Szopa, S., Turquety, S., 2012. Assimilation of IASI satellite CO fields into a global chemistry transport model for validation against aircraft measurements. Atmos. Chem. Phys. 12, 4493–4512. https://doi.org/10.5194/acp-12-4493-2012.

Krishna Moorthy, K., Suresh Babu, S., Manoj, M.R., Satheesh, S.K., 2013. Buildup of aerosols over the Indian Region. Geophys. Res. Lett. 40, 1011–1014. https://doi.org/10.1002/grl.50165.

Krotkov, N.A., McLinden, C.A., Li, C., Lamsal, L.N., Celarier, E.A., Marchenko, S.V., Swartz, W.H., Bucsela, E.J., Joiner, J., Duncan, B.N., Boersma, K.F., Veefkind, J.P., Levelt, P.F., Fioletov, V.E., Dickerson, R.R., He, H., Lu, Z., Streets, D.G., 2016. Aura OMI observations of regional SO2 and NO2 pollution changes from 2005 to 2015. Atmos. Chem. Phys. 16, 4605–4629. https://doi.org/10.5194/acp-16-4605-2016.

Kulawik, S.S., Worden, J., Eldering, A., Bowman, K., Gunson, M., Osterman, G.B., Zhang, L., Clough, S., Shephard, M.W., Beer, R., 2006. Implementation of cloud retrievals for Tropospheric Emission Spectrometer (TES) atmospheric retrievals: part 1. Description and characterization of errors on trace gas retrievals. J. Geophys. Res. 111, D24204. https://doi.org/10.1029/2005JD006733.

Lack, D.A., Tie, X.X., Bofinger, N.D., Wiegand, A.N., Madronich, S., 2004. Seasonal variability of secondary organic aerosol: A global modelling study. J. Geophys. Res. 109, D03203 https://doi.org/10.1029/2003JD003418.

Lelieveld, J., Gromov, S., Pozzer, A., Taraborrelli, D., 2016. Global tropospheric hydroxyl distribution, budget and reactivity. Atmos. Chem. Phys. 16, 12477–12493. https://doi.org/10.5194/acp-16-12477-2016.

Levy, R.C., Mattoo, S., Munchak, L.A., Remer, L.A., Sayer, A.M., Patadia, F., Hsu, N.C., 2013. The collection 6 MODIS aerosol products over land and ocean. Atmos. Meas. Tech. 6 (11), 2989–3034. https://doi.org/10.5194/amt-6-2989-2013.

Levy, R.C., Mattoo, S., Sawyer, V., Shi, Y., Colarco, P.R., Lyapustin, A.I., Wang, Y., Remer, L.A., 2018. Exploring systematic offsets between aerosol products from the two MODIS sensors. Atmos. Meas. Tech. 11, 4073–4092. https://doi.org/10.5194/amt-11-4073-2018.

Li, C., McLinden, C., Fioletov, V., Krotkov, N., Carn, S., Joiner, J., Streets, D., He, H., Ren, X., Li, Z., Dickerson, R.R., 2017. India is overtaking china as the world's largest emitter of anthropogenic sulfur dioxide. Sci. Rep. 7, 14304. https://doi.org/10.1038/s41598-017-14639-8.

Li, K., Jacob, D.J., Liao, H., Shen, L., Zhang, Q., Bates, K.H., 2019. Anthropogenic drivers of 2013–2017 trends in summer surface ozone in China. Proc. Natl. Acad. Sci. U. S. A. 116, 422–427. https://doi.org/10.1073/pnas.1812168116.

Li, M., Wang, T., Xie, M., Li, S., Zhuang, B., Chen, P., Huang, X., Han, Y., 2018. Agricultural fire impacts on ozone photochemistry over the Yangtze River Delta region, East China. J. Geophys. Res.-Atmos. 123 (12), 6605–6623. https://doi.org/10.1029/2018JD028582.

Liu, J., Mauzerall, D.L., Chen, Q., Zhang, Q., Song, Y., Peng, W., Klimont, Z., Qiu, X., Zhang, S., Hu, M., Lin, W., Smith, K.R., Zhu, T., 2016. Air pollutant emissions from Chinese households: A major and underappreciated ambient pollution source. P. Natl. Acad. Sci. USA 113 (28), 7756–7761. https://doi.org/10.1073/pnas.1604537113.

Luo, M., Rinsland, C., Fisher, B., Sachse, G., Diskin, G., Logan, J., Worden, H., Kulawik, S., Osterman, G., Eldering, A., Herman, R., Shephard, M., 2007. TES carbon monoxide validation with DACOM aircraft measurements during INTEX-B 2006. J. Geophys. Res. 112, D24S48. https://doi.org/10.1029/2007JD008803.

Luo, M., Read, W., Kulawik, S., Worden, J., Livesey, N., Bowman, K., Herman, R., 2013. Carbon monoxide (CO) vertical profiles derived from joined TES and MLS measurements. J. Geophys. Res.-Atmos. 118 (18), 10,601–10,613.

Luo, M., Shephard, M.W., Cady-Pereira, K.E., Henze, D.K., Zhu, L., Bash, J.O., Pinder, R. W., Capps, S.L., Walker, J.T., Jones, M.R., 2015. Satellite observations of tropospheric ammonia and carbon monoxide: Global distributions, regional correlations and comparisons to model simulations. Atmos. Environ. 106, 262–277, 4.

Luo, Y., Zheng, X., Zhao, T., Chen, J., J., 2014. A climatology of aerosol optical depth over China from recent 10 years of MODIS remote sensing data. Int. J. Climatol. 34 (3), 863–870. https://doi.org/10.1002/joc.3728.

Mann, H.B., 1945. Non-parametric test against trend. Econometrica 13, 245–259. https://doi.org/10.2307/1907187.

Manoj, M.R., Satheesh, S.K., Moorthy, K.K., Gogoi, M.M., Babu, S.S., 2019. Decreasing trend in black carbon aerosols over the Indian region. Geophys. Res. Lett. 46, 2903–2910. https://doi.org/10.1029/2018GL081666.

McClure, C.D., Jaffe, D.A., 2018. US particulate matter air quality improves except in wildfire-prone Areas. P. Natl. Acad. Sci. USA 115 (31), 7901–7906. https://doi.org/10.1073/pnas.1804353115.

McDonald, B.C., Gentner, D.R., Goldstein, A.H., Harley, R.A., 2013. Long-term trends in motor vehicle emissions in U.S. urban areas. Environ. Sci. Technol. 47, 10022–10031. https://doi.org/10.1021/es401034z.

Mehta, M., Singh, R., Singh, A., Singh, N., Anshumali, 2016. Recent global aerosol optical depth variations and trends - A comparative study using MODIS and MISR level 3 datasets. Remote Sens. Environ. 181, 137–150. https://doi.org/10.1016/j.rse.2016.04.004.

Myhre, G., Shindell, D., Bréon, F.-M., Collins, W., Fuglestvedt, J., Huang, J., Koch, D., Lamarque, J.-F., Lee, D., Mendoza, B., Nakajima, T., Robock, A., Stephens, G., Takemura, T., Zhang, H., 2014. Climate Change 2013: The Physical Science Basis. In: Contribution of Working Group I to the Fifth Assessment Report of the Intergovernmental Panel on Climate Change, chapter Anthropogenic and Natural Radiative Forcing. Cambridge University Press, pp. 659–740.

Novelli, P.C., Masarie, K.A., Lang, P.M., Hall, B.D., Myers, R.C., Elkins, J.W., 2003. Reanalysis of tropospheric CO trends: Effects of the 1997–1998 wildfires. J. Geophys. Res.-Atmos. 108, 4464. https://doi.org/10.1029/2002jd003031.

Pandey, A., Sadavarte, P., Rao, A.B., Venkataraman, C., 2014. Trends in multi-pollutant emissions from a technology-linked inventory for India: II. Residential, agricultural and informal industry sectors. Atmos. Environ. 99, 341–352. https://doi.org/10.1016/j.atmosenv.2014.09.080.

Platnick, S., King, M., Hubanks, P., 2017. MODIS Atmosphere L3 Monthly Product. In: NASA MODIS Adaptive Processing System, Goddard Space Flight Center. https://doi.org/10.5067/MODIS/MOD08_M3.006.

Pommier, M., Law, K.S., Clerbaux, C., Turquety, S., Hurtmans, D., Hadji-Lazaro, J., Coheur, P.-F., Schlager, H., Ancellet, G., Paris, J.-D., Nédélec, P., Diskin, G.S., Podolske, J.R., Holloway, J.S., Bernath, P., 2010. IASI carbon monoxide validation over the Arctic during POLARCAT spring and summer campaigns. Atmos. Chem. Phys. 10, 10655–10678. https://doi.org/10.5194/acp-10-10655-2010.

Prather, M.J., 2007. Lifetimes and time scales in atmospheric chemistry. Phil. Trans. R. Soc. A 365, 1,705–1,726. https://doi.org/10.1098/rsta.2007.2040.

Proestakis, E., Amiridis, V., Marinou, E., Georgoulias, A.K., Solomos, S., Kazadzis, S., Chimot, J., Che, H., Alexandri, G., Binietoglou, I., Daskalopoulou, V., Kourtidis, K.A., de Leeuw, G., van der A, R.J., 2018. Nine-year spatial and temporal evolution of desert dust aerosols over South and East Asia as revealed by CALIOP. Atmos. Chem. Phys. 18 (2), 1337–1362. https://doi.org/10.5194/acp-18-1337-2018.

Qu, Z., Henze, D.K., Li, C., Theys, N., Wang, Y., Wang, J., Wang, W., Han, J., Shim, C., Dickerson, R.R., Ren, X., 2019. SO_2 emission estimates using OMI SO_2 retrievals for 2005–2017. J. Geophys. Res.-Atmos. 124, 8336–8359. https://doi.org/10.1029/2019JD030243.

Ramanathan, V., Carmichael, G., 2008. Global and regional climate changes due to black carbon. Nat. Geosci. 1, 221–227. https://doi.org/10.1038/ngeo156.

Reuter, M., Buchwitz, M., Hilboll, A., Richter, A., Schneising, O., Hilker, M., Heymann, J., Bovensmann, H., Burrows, J.P., 2014. Decreasing emissions of NOx relative to CO2 in East Asia inferred from satellite observations. Nat. Geosci. 7, 792–795. https://doi.org/10.1038/ngeo2257.

Revercomb, H., Strow, L., 2018. Suomi NPP CrIS Level 1B Full Spectral Resolution V2, Accessed from GES DISC February 2019. https://doi.org/10.5067/9NPOTPIPLMAW.

Rinsland, C.P., Luo, M., Logan, J.A., Beer, R., Worden, H., Kulawik, S.S., Rider, D., Osterman, G., Gunson, M., Eldering, A., Goldman, A., Shephard, M., Clough, S.A., Rodgers, C., Lampel, M., Chiou, L., 2006. Nadir measurements of carbon monoxide distributions by the Tropospheric Emission Spectrometer instrument onboard the Aura Spacecraft: Overview of analysis approach and examples of initial results. Geophys. Res. Lett. 33, L22806 https://doi.org/10.1029/2006GL027000.

Sadavarte, P., Venkataraman, C., 2014. Trends in multi-pollutant emissions from a technology-linked inventory for India: I. Industry and transport sectors. Atmos. Environ. 99, 353–364. https://doi.org/10.1016/j.atmosenv.2014.09.081.

Sayer, A.M., Munchak, L.A., Hsu, N.C., Levy, R.C., Bettenhausen, C., Jeong, M.-J., 2014. MODIS Collection 6 aerosol products: comparison between Aqua's e-Deep Blue, Dark Target, and "merged" data sets, and usage recommendations. J. Geophys. Res.-Atmos. 119, 13965–13989. https://doi.org/10.1002/2014JD022453.

Schultz, M.G., Akimoto, H., Bottenheim, J., Buchmann, B., Galbally, I.E., Gilge, S., Helmig, D., Koide, H., Lewis, A.C., Novelli, P.C., Plass-Dülmer, C., Ryerson, T.B., Steinbacher, M., Steinbrecher, R., Tarasova, O., Tørseth, K., Thouret, V., Zellweger, C., 2015. The Global Atmosphere Watch reactive gases measurement network. Elem Sci Anth 3, 67 doi:10.12952.

Sen, P.K., 1968. Estimates of regression coefficient based on Kendall's tau. J. Am. Stat. Assoc. 63, 324.

Shine, K.P., Barnett, J.J., Randel, W.J., 2008. Temperature trends derived from Stratospheric Sounding Unit radiances: The effect of increasing CO2 on the weighting function. Geophys. Res. Lett. 35, L02710 https://doi.org/10.1029/2007GL032218.

Streets, D.G., Zhang, Q., Wang, L., He, K., Hao, J., Wu, Y., Tang, Y., Carmichael, G.R., 2006. Revisiting China's CO emissions after the Transport and Chemical Evolution over the Pacific (TRACE-P) mission: Synthesis of inventories, atmospheric modeling, and observations. J. Geophys. Res. Atmos. 111 (D14) https://doi.org/10.1029/2006JD007118.

Strode, S.A., Pawson, S., 2013. Detection of carbon monoxide trends in the presence of interannual variability. J. Geophys. Res. Atmos. 118, 12,257–12,273. https://doi.org/10.1002/2013JD020258.

Strode, S.A., Worden, H.M., Damon, M., Douglass, A.R., Duncan, B.N., Emmons, L.K., Lamarque, J.-F., Manyin, M., Oman, L.D., Rodriguez, J.M., Strahan, S.E., Tilmes, S., 2016. Interpreting space-based trends in carbon monoxide with multiple models. Atmos. Chem. Phys. 16, 7285–7294. https://doi.org/10.5194/acp-16-7285-2016.

Susskind, J., Barnet, C.D., Blaisdell, J.M., 2003. Retrieval of atmospheric and surface parameters from AIRS/AMSU/HSB data in the presence of clouds. IEEE Trans. Geosci. Remote Sens. 41 (2), 390–409. https://doi.org/10.1109/TGRS.2002.808236.

Tang, W., Arellano, A.F., Gaubert, B., Miyazaki, K., Worden, H.M., 2019. Satellite data reveal a common combustion emission pathway for major cities in China. Atmos. Chem. Phys. 19, 4269–4288. https://doi.org/10.5194/acp-19-4269-2019.

Theil, H., 1950. A rank invariant method of linear and polynomial regression analysis, i, ii, iii. Proc. Koninklijke Nederl. Akad. Wet. Ser. A Math. Sci. 53, 1397–1412.

Unger, N., Shindell, D.T., Koch, D.M., Streets, D.G., 2006. Cross influences of ozone and sulfate precursor emissions changes on air quality and climate. Proc. Natl. Acad. Sci. U. S. A. 103 (12), 4377–4380. https://doi.org/10.1073/pnas.0508769103.

van der A, R.J., Mijling, B., Ding, J., Koukouli, M.E., Liu, F., Li, Q., Mao, H., Theys, N., 2017. Cleaning up the air: effectiveness of air quality policy for SO2 and NOx emissions in China. Atmos. Chem. Phys. 17, 1775–1789. https://doi.org/10.5194/acp-17-1775-2017.

van der Werf, G.R., Randerson, J.T., Giglio, L., Collatz, G.J., Mu, M., Kasibhatla, P.S., Morton, D.C., DeFries, R.S., Jin, Y., van Leeuwen, Y.T.T., 2010. Global fire emissions and the contribution of deforestation, savanna, forest, agricultural, and peat fires (1997-2009). Atmos. Chem. Phys. 10, 11707–11735. https://doi.org/10.5194/acp-10-11707-2010.

Veefkind, J.P., Boersma, K.F., Wang, J., Kurosu, T.P., Krotkov, N., Chance, K., Levelt, P. F., 2011. Global satellite analysis of the relation between aerosols and short-lived trace gases. Atmos. Chem. Phys. 11, 1255–1267. https://doi.org/10.5194/acp-11-1255-2011.

Voss, K.K., Evan, A.T., 2020. A new satellite-based global climatology of dust aerosol optical depth. J. Appl. Meteorol. Climatol. 59, 83–102. https://doi.org/10.1175/JAMC-D-19-0194.1.

Wang, S., Hao, J., 2012. Air quality management in China: Issues, challenges, and options. J. Environ. Sci. 24, 2–13. https://doi.org/10.1016/S1001-0742(11)60724-9.

Wang, Y., Wang, J., 2020. Tropospheric SO2 and NO2 in 2012–2018: Contrasting views of two sensors (OMI and OMPS) from space. Atmos. Environ. 223, 117214. https://doi.org/10.1016/j.atmosenv.2019.117214.

Warner, J.X., McCourt Comer, M., Barnet, C., McMillan, W.W., Wolf, W., Maddy, E., Sachse, G., 2007. A comparison of satellite tropospheric carbon monoxide measurements from AIRS and MOPITT During INTEX-NA. J. Geophys. Res. 112, D12S1. https://doi.org/10.1029/2006JD007925.

Warner, J.X., Wei, Z., Strow, L.L., Barnet, C.D., Sparling, L.C., Diskin, G., Sachse, G., 2010. Improved agreement of AIRS tropospheric carbon monoxide products with other EOS sensors using optimal estimation retrievals. Atmos. Chem. Phys. 10, 9521–9533. https://doi.org/10.5194/acp-10-9521-2010.

Weatherhead, E.C., Reinsel, G.C., Tiao, G.C., Meng, X.-L., Choi, D., Cheang, W.-K., Keller, T., DeLuisi, J., Wuebbles, D.J., Kerr, J.B., Miller, A.J., Oltmans, S.J., Frederick, J.E., 1998. Factors affecting the detection of trends: Statistical considerations and applications to environmental data. J. Geophys. Res. 103 (D14), 17149–17161. https://doi.org/10.1029/98JD00995.

Wei, J., Peng, Y., Guo, J., Sun, L., 2019a. Performance of MODIS Collection 6.1 Level 3 aerosol products in spatial-temporal variations over land. Atmos. Environ. 206, 30–44. https://doi.org/10.1016/j.atmosenv.2019.03.001.

Wei, J., Peng, Y., Mahmood, R., Sun, L., Guo, J., 2019b. Intercomparison in spatial distributions and temporal trends derived from multi-source satellite aerosol products. Atmos. Chem. Phys. 19, 7183–7207. https://doi.org/10.5194/acp-19-7183-2019.

Witek, M.L., Diner, D.J., Garay, M.J., 2016. Satellite assessment of sea spray aerosol productivity: Southern Ocean case study. J. Geophys. Res. Atmos. 121, 872–894. https://doi.org/10.1002/2015JD023726.

Worden, H.M., Deeter, M.N., Frankenberg, C., George, M., Nichitiu, F., Worden, J., Aben, I., Bowman, K.W., Clerbaux, C., Coheur, P.F., de Laat, A.T.J., Detweiler, R., Drummond, J.R., Edwards, D.P., Gille, J.C., Hurtmans, D., Luo, M., Martínez-Alonso, S., Massie, S., Pfister, G., Warner, J.X., 2013. Decadal record of satellite carbon monoxide observations. Atmos. Chem. Phys. 13, 837–850. https://doi.org/10.5194/acp-13-837-2013.

Worden, J., Liu, X., Bowman, K., Chance, K., Beer, R., Eldering, A., Gunson, M., Worden, H., 2007. Improved tropospheric ozone profile retrievals using OMI and TES radiances. Geophys. Res. Lett. 34, L01809 https://doi.org/10.1029/2006GL027806.

Wu, Y., Han, Y., Voulgarakis, A., Wang, T., Li, M., Wang, Y., Xie, M., Zhuang, B., Li, S., 2017. An agricultural biomass burning episode in eastern China: Transport, optical properties, and impacts on regional air quality. J. Geophys. Res.-Atmos. 122 (4), 2304–2324. https://doi.org/10.1002/2016JD025319.

Yang, H., Waugh, D.W., Orbe, C., Patra, P.K., Jöckel, P., Lamarque, J.-F., Tilmes, S., Kinnison, D., Elkins, J.W., Dlugokencky, E.J., 2019. Evaluating simulations of interhemispheric transport: Interhemispheric exchange time versus SF6 age. Geophys. Res. Lett. 46, 1113–1120. https://doi.org/10.1029/2018GL080960.

Yin, Y., Chevallier, F., Ciais, P., Broquet, G., Fortems-Cheiney, A., Pison, I., Saunois, M., 2015. Decadal Trends in Global CO Emissions as Seen by MOPITT. Atmos. Chem. Phys. Discuss. 15 (10), 14505–14547. https://doi.org/10.5194/acpd-15-14505-2015.

Yoon, J., Pozzer, A., Hoor, P., Chang, D.Y., Beirle, S., Wagner, T., Schloegl, S., Lelieveld, J., Worden, H.M., 2013. Technical Note: Temporal change in averaging kernels as a source of uncertainty in trend estimates of carbon monoxide retrieved from MOPITT. Atmos. Chem. Phys. 13, 11307–11316. https://doi.org/10.5194/acp-13-11307-2013.

Zeng, G., Wood, S.W., Morgenstern, O., Jones, N.B., Robinson, J., Smale, D., 2012. Trends and variations in CO, C_2H_6, and HCN in the Southern Hemisphere point to the declining anthropogenic emissions of CO and C_2H_6. Atmos. Chem. Phys. 12, 7543–7555. https://doi.org/10.5194/acp-12-7543-2012.

Zhang, X., Liu, J., Han, H., Zhang, Y., Jiang, Z., Wang, H., Meng, L., Li, Y.C., Liu, Y., 2020. Satellite-observed variations and trends in carbon monoxide over asia and their sensitivities to biomass burning. Remote Sens. 12, 830. https://doi.org/10.3390/rs12050830.

Zheng, B., Tong, D., Li, M., Liu, F., Hong, C., Geng, G., Li, H., Li, X., Peng, L., Qi, J., Yan, L., Zhang, Y., Zhao, H., Zheng, Y., He, K., Zhang, Q., 2018a. Trends in China's anthropogenic emissions since 2010 as the consequence of clean air actions. Atmos. Chem. Phys. 18, 14095–14111. https://doi.org/10.5194/acp-18-14095-2018.

Zheng, B., Chevallier, F., Ciais, P., Yin, Y., Deeter, M.N., Worden, H.M., Wang, Y., Qiang, Zhang, He, K., 2018b. Rapid decline in carbon monoxide emissions and export from East Asia between years 2005 and 2016. Environ. Res. Lett. 13 (4), 044007 https://doi.org/10.1088/1748-9326/aab2b3.

Zheng, B., Chevallier, F., Yin, Y., Ciais, P., Fortems-Cheiney, A., Deeter, M.N., Parker, R. J., Wang, Y., Worden, H.M., Zhao, Y., 2019. Global atmospheric carbon monoxide budget 2000–2017 inferred from multi-species atmospheric inversions. Earth Syst. Sci. Data 11, 1411–1436. https://doi.org/10.5194/essd-11-1411-2019.